SYNTHESIS AND CHARACTERIZATION OF PLASMONIC-MAGNETIC Au-Co
MULTILAYERED NANORODS

by

AKSHAY HANDE

Presented to the Faculty of the Graduate School of

The University of Texas at Arlington

in Partial Fulfillment of the Requirements

for the Degree of

MASTER OF SCIENCE

IN MATERIALS SCIENCE AND ENGINEERING

THE UNIVERSITY OF TEXAS AT ARLINGTON

May 2016

Acknowledgements

I have deep appreciation for my thesis advisor, Dr. Yaowu Hao, who has always guided and supported me throughout my time here at UT Arlington. He has never failed to clear my queries whether it be studies or research. I would like to express special thanks to my thesis defense committee members, Dr. Choong-Un Kim and Dr. Fuqiang Liu, for their suggestions and advice regarding my research.

I would also like to thank my lab mates, Aaron, sina, chris, Richie, Sandesh and koi for their friendship and helpful discussions.

I would also like to thank our departmental assistants, Beth and Jennifer, for their timely help and support in all activities every single day. I am thankful to the staff at Nanofab for providing the equipment necessary for my research.

Finally, I am very lucky for having such a great family and friends who encourage me at every turn in my life to finish what I start.

ABSTRACT

Au nanoparticles (AuNPs) and superparamagnetic iron oxide nanoparticles (SPIONs), in various forms, are considered as biocompatible and are of great interest for diagnostic imaging and therapeutic applications. Biomedical applications of AuNPs originate from the surface plasmon resonance (SPR) effect. In order to tune the SPR wavelength to the near infrared (NIR) region which is required for deep light penetration for in vivo applications, various types of AuNPs such as nanorods, nanoprisms, [1] nanoshells and nanocages have been developed and investigated. SPIONs have also been explored extensively for biomedical applications, including magnetic cell separation, contrast enhancement agents for magnetic resonance imaging (MRI), targeted drug and gene delivery, hyperthermia treatment, biophysical studies, and bio sensing. In recent years, combining SPIONs with Au to form a composite multifunctional nanoparticles has attracted considerable attention. However, the effort has been mostly limited on coating iron oxide particles with a thin layer of Au. By such an approach, it is difficult, if not impossible, to tune the SPR wavelengths to the NIR region. Reported core/shell particles usually have their SPR in the visible light range (from 500 nm to 600 nm), which limits their optical functions for in vivo applications.

The Au-Co multilayered nanoparticles made in this study have the benefit of high magnetization, small remanence and SPR peak's presence in the NIR spectrum range. These particles were made using template synthesis technique. Anodic aluminum oxide (AAO) membrane which possess ~80 nm through channels is used as template. AAO membranes are successfully fabricated using an anodization process. Multilayered Au/Co nanoparticles are electrodeposited into the channels following the

electrodeposition of Cu rod which serve as sacrificial layer for releasing the multilayered particles into the solution.

The magnetic and optical properties of multilayered nanoparticles are characterized, and compared with theoretical calculation and computer simulation. It has been found that the multilayered nanorods have a single peak at around 620 nm (disc like Co segments) and at 590 nm (rod like Co segments), which suggests a blue shift if the inter Au layer distance increases (i.e. increase in Co layer thickness). The easy axis was determined as along the rod axis and along the diameter for rod like and disc like Co segments by using VSM measurements which can be credited to their shape anisotropy. The remanence and coercivity (<100 Oe) in the measured hysteresis loops are very low which is beneficial for biomedical applications. The theoretical calculations confirmed lower values of shape anisotropy energy along their easy axes than along other axes. The FDTD simulation results for the nanorods, which were similar to experimental results, showed a single peak around 530nm when illuminated along the axis of the rod without considering water as surrounding medium. The rods with an extra Au and Co layer (rod with 11 layers) showed no noticeable difference for both SPR and magnetic properties when compared to rods with lesser Au and Co layers (i.e. rod with 9 layers).

The multilayer nanorods have absorption peaks in NIR range which are tunable by changing individual layer thicknesses and they have very high magnetization with low remanence and coercivity which makes them suitable for biomedical applications such as MRI imaging, cancer therapy etc. Thus, multiple Au disc separated by alternate Co layers give dual properties (plasmonic and magnetic) in a single entity with benefit of easy tuning by a simple change of thickness.

TABLE OF CONTENTS

TABLE OF FIGURES

1   INTRODUCTION

In the last decade an intense study has been done on Gold nanoparticles (AuNPs) and superparamagnetic iron oxide nanoparticles (SPIONs) [2, 3]. They are considered as biocompatible and are of great interest for diagnostic imaging and therapeutic applications. The magnetic nanoparticles have been explored extensively for biomedical applications [4]. The various applications for the nanoparticles include magnetic cell separation [5], contrast enhancement agents for magnetic resonance imaging (MRI) [6, 7], targeted drug and gene delivery [8-10], hyperthermia treatment [6, 11-13], biophysical studies [14-17], and bio sensing.

Biomedical applications of AuNPs originate from the surface plasmon resonance (SPR) effect, a strong enhancement of absorption and scattering of light when it has the same frequency as that of the SPR frequency, which has been utilized for photo thermal ablation treatment and optical imaging. To tune the SPR wavelength to the near infrared (NIR) region, which is commonly regarded as a 'clear window' for deep tissue penetration of light, various types of Au nanoparticles such as nanorods,[18] nanoprisms,[1] nanoshells,[19, 20] and nanocages[21, 22] have been developed and investigated.

In recent years, combining SPIONs with Au to form a composite multifunctional nanoparticles has attracted considerable attention.[23-27] To date, the effort has been mostly limited on coating iron oxide particles with a thin layer of Au, where the Au shell not only provides convenient anchorage sites for functionalization of biomolecules through the well-established Au-thiol conjugation

procedure but also protects SPIONs from dissolution and aggregation. However, by such an approach, it is difficult, if not impossible, to tune the SPR wavelengths to the NIR region. Reported core/shell particles usually have their SPR in the visible light range (from 500 nm to 600 nm), which limits their optical functions for in vivo applications.

Fe oxide nanoparticles are extensively studied for their magnetic properties and have been an obvious choice for various applications until recently. But the saturation magnetization that it can achieve, 80 emu/g, is relatively low when compared with other metallic magnetic materials like Co (160 emu/g), FeCo (235 emu/g) or Fe (190 emu/g) and so moving on to elements like Co could be an efficient choice for the future. The magnetization achieved by the iron oxide nanoparticles might not be sufficient for certain application like cell and DNA mechanics, drug and gene targeted delivery, magnetic bio sensing and bio separation as there is a minimum magnetization requirement for these applications to work effectively. Even though the increase in size of the particle can increase the amount of magnetic moment, it is not always applicable as increasing the size beyond a certain limit leads to a loss of superparamagnetic properties of the nanoparticles. Superparamagnetic properties are essential for the biomedical applications as it requires the particles to reach saturation magnetization at lower values of applied field and have lower remanence when the external field is removed. Thus, Co can replace Fe oxide nanoparticles for certain applications and give higher magnetization values at relatively smaller particle sizes. The available magnetic nanoparticles are either too small (<20 nm) (probably without sufficient

magnetic moment) or too big (>100nm) (probably without superparamagnetism) for many biomedical applications. The Au-Co multilayered nanoparticles made in this study should have the benefit of high magnetic moment at size less than 100 nm. This should fill the size gap (20nm to 100nm) of magnetic nanoparticles for biomedical applications as mentioned earlier.

The Au layer in these particles possess special SPR properties which can be used for biomedical applications. The SPR can simply be considered as enriched absorption of electromagnetic radiation due to the interaction between an incident electromagnetic radiation light and the electron sea in a metal particle (especially Au). It can also be described in detail as, when an electromagnetic wave is incident on an Au nanoparticle it sets the electron sea in the particle in oscillation with its own oscillation frequency. The quanta of this oscillation is termed as a plasmon. When the frequency of this oscillation (plasmon oscillation) matches with frequency of incident radiation then there is a strong absorption of the incident radiation. The SPR frequencies of Au are present in visible and NIR range and so the particles suspended in water have an intense visible color. Part of the absorbed incident light that is radiated back, but in other directions, with the same frequency is termed as scattering. SPR frequency and the amount of scattering vs absorption out of the incident source light depend upon various factors like size and shape of the particles, inter particle interactions (coupling effect) and the dielectric properties of the surrounding medium.

The theoretical studies have suggested that the discs have two modes of plasmonic vibrations – longitudinal (along the axis of the disc) and transverse

3

(along the surface or in the plane of the disc). The transverse mode is more pronounced than the longitudinal mode and so sometimes longitudinal peak can be neglected or is even hard to distinguish from the noise. It is also found that with the increase in the diameter of the disc the transverse peak moves to the red side (i.e. to the higher wavelength side) of the spectrum. The disc shaped Au layers in the multilayered nanoparticles would provide the special SPR properties to the nanoparticles.

Thus, the multilayered particles of alternate Au and Co layers have dual plasmonic and magnetic properties. This dual nature can be helpful in biomedical applications as the magnetic properties would lead to enhancement of the contrast in the MRI imaging of the affected region in the patient's body and the SPR properties could be used for cancer therapy. Thus with the help of multilayered nanoparticles, cancer tumors can be tracked and observed under MRI, in situ, and later on can be used for therapeutic treatment.

This thesis describes the synthesis technique and characterization (particularly SEM, VSM, UV-Vis spectroscopy and FDTD simulation) of the multilayered Au-Co nanoparticles. The particles were made using template synthesis technique in large quantities. The template used here is anodic aluminum oxide (AAO) membrane and the fabrication of AAO membrane is also described.

2   BACKGROUND INFORMATION

2.1   OPTICAL PROPERTIES OF AuNPs

When an electromagnetic wave from a light source interacts with conduction Electron Sea around the gold nanostructures, the conduction electrons oscillate collectively at a certain frequency. If this oscillation frequency is similar to the frequency of the light source electromagnetic wave then there is a resonance and large amount of light is absorbed and scattered. This phenomenon is termed as the surface plasmonic resonance effect (SPR)[13]. The oscillations of electrons around the positive lattice ions are driven by the electric field of the light source. The important application of this phenomenon is that the absorbed energy is converted to thermal energy because of the friction between the oscillating electrons and the outside medium which can be utilized to kill the cancer cells. The healthy tissue can outlive this rise in temperature and the cancer cells will degenerate as they are more vulnerable to heat than the regular cells. This particular application of SPR effect is termed as photo thermal therapy. The incident photons that are not absorbed by the nanoparticles is termed as scattering of light. A plasmon can be understood as a packet or quanta of electron cloud oscillations around the nanoparticles (just like photons are the quanta of light or phonons are the quanta of mechanical vibrations). The frequency of the scattered light is same as that of the incident light. The scattering and absorption is together termed as extinction.

For biomedical applications, the absorption is expected to be in the range of 800nm to 1200nm as deeper penetration of the incident light source can be

achieved of the incident light in this wavelength range in to the soft tissues (i.e. blood and other biological samples are transparent in NIR region) without causing any damage to them whatsoever. When the particles are close to each other or when they aggregate to each other the peak position shifts, depending on the type of particles, to the lower or higher wavelength side of the wavelength spectrum. This is termed as plasmonic coupling effect and it is the basic principle for colorimetric sensing where depending upon the distance between the particles the color of the solution changes. Coupling is caused by Plasmon to Plasmon interaction of particles when close to each other. Also, the Au Nano particles enhance the local electromagnetic field by large amounts, due to SPR effect, and so are used as substrates for surface enhanced Raman scattering (SERS).

When absorption is analyzed with respect to the change in the wavelength of the source (like in UV Vis measurements), the absorption peak can be seen at a certain wavelength but absorption fades at other wavelengths of the source. This spectra can also be determined by calculating solution to the Maxwell's partial differential equations. The very first efforts towards this analysis were done by Gustav Mie [28] for spherical particles in 1908. Which was modified by Richard Gans for spheroids later on[29]. However the exact solution to Maxwell's equation are available only for spheres, concentric spherical shells, spheroids and infinite cylinders. So an approximation is necessary for other shapes to solve the Maxwell's equation which can be done by using discrete dipole approximation (DDA). Numerous different types of nanoparticles can be used in applications like

colorimetric sensing, surface enhanced Raman scattering (SERS) and biomedical application etc and so approximation is getting more necessary recently.

Mie theory, unlike Rayleigh's theory, applies to absorbing or non-absorbing material and so is widely used for spherical metallic particles. It is an exact solution to Maxwell's electromagnetic field equations for a plane wave and particle interaction. Ignoring the higher order terms in the Maxwell's equations and using mie theory, assuming the particles are very small. i.e. 2R<<λ, for spherical particles we get equation (1) for calculating the coefficient of extinction below [13],

$$C_{ext} = \frac{24\pi^2 R^3 \, \varepsilon_m^{\frac{3}{2}}}{\lambda} \frac{\varepsilon_2}{(\varepsilon_1 + 2\varepsilon_m)^2 + \varepsilon_2^2} \qquad (1)$$

Here,

ε_m is the dielectric constant of the surrounding medium.

ε (complex dielectric constant of the material) = $\varepsilon_1 + i\,\varepsilon_2$.

Resonance happens at $\varepsilon_1 = -2\,\varepsilon_m$.

The absorption peaks, for spherical particles, move to the red side (higher wavelength side) with the increase in their particle size. Also, the peak gets broader with size of the particles which can be credited to increased radiation dampening which can be seen in Fig (1).

The shape can drastically change the absorption properties (.i.e. the surface plasmonic properties) of the particles. Gans modified the boundary conditions present in Mie theory so that it could be used for nanorods. He predicted that the

rods should show two modes of absorption (longitudinal and transverse) due to the possibility of different orientations of the rod to the incident electromagnetic light source. The extinction cross section can be determined by equation (2).
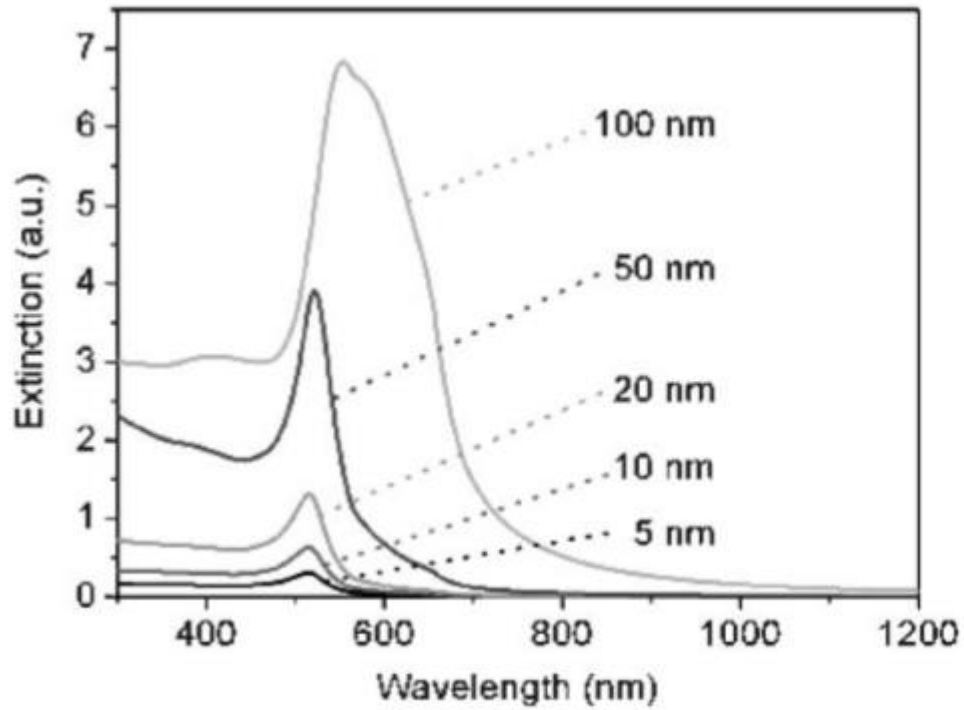
Figure 1. The extinction spectra variation with particle size as calculated using Mie theory.

$$C_{ext} = \frac{2\pi V}{3\lambda} \varepsilon_m^{3/2} \sum_j \frac{(1/P_j^2)\varepsilon_2}{\left(\varepsilon_1 + \frac{1-P_j}{P_j}\varepsilon_m\right)^2 + \varepsilon_2^2} \qquad (2)$$

Here,

V = volume of the rod

P_j = depolarization factor where j = A, B, C; A > B = C, A = length, B = C = width

which gives equation (3) and equation (4),

$$P_A = \frac{1-e^2}{e^2}\left[\frac{1}{2e}\ln\left(\frac{1+e}{1-e}\right) - 1\right] \qquad (3)$$

$$P_B = P_C = \frac{1-P_A}{2} \qquad (4)$$

Here,

$e^2 = 1 - \xi^{-2}$ and ξ = A/B i.e. aspect ratio.
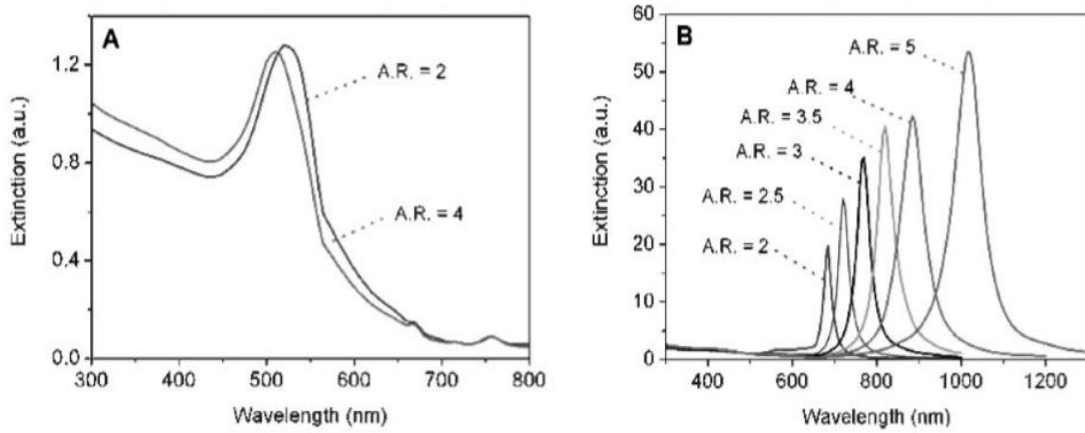
Figure 2. Extinction spectra of rods estimated using DDA technique for different aspect ratios with 20 nm cross section width for (A) transverse (B) longitudinal mode

Discrete Dipole Approximation (DDA) is also be used to determine the extinction cross section of Nano rods which can also be extended to arbitrarily shaped Nano particles. In DDA calculations the particles are considered as an array of consecutive cells with point dipoles whose moments have their individual position vectors and local electromagnetic fields [13]. The extinction spectra calculated for Au nanorods by DDA approximation is given in fig 2(A) and fig 2(B) for both transverse and longitudinal modes. In the transverse mode the electron cloud oscillates in perpendicular direction to that of the rod's length whereas in longitudinal mode the electron cloud oscillates in direction parallel to the length of the rod. It can be seen that for longitudinal mode the peak shifts to red side of spectrum with the rise in aspect ratio (fig2.B) and for transverse mode it shifts to blue side by a small amount (fig 2.A). The SPR peak can be tuned in visible to near infra-red regions for Nano rods with different aspect ratios [30]. The retardation effect affects the plasmonic response negatively if the nanorod have diameters are greater than 100nm. The DDA can also help us to compare how much absorption is there out of the total extinction for the spherical and rod nanoparticles which can be seen clearly in fig3 (A) and fig3 (B). It is noteworthy to mention that the absorption cross section is quite large than scattering cross section for those particles [13]. There is a linear relationship between the longitudinal SPR peak wavelength and the aspect ratio of Nano rods [31] [fig 4(c)]

in visible range of the wavelength spectrum. The different shapes of the rod heads, with the same lengths and diameters, have different SPR peak positions.

For nanorods, the SPR peak for the longitudinal mode of vibration is present to the red side of the transverse mode due to the longer path of oscillation for longitudinal mode [31]. Both longitudinal and transverse modes are dipolar resonances and so they can be excited by an external incident plane wave. This is not true for particles that have more than two modes of oscillation (like quadrupolar or octupolar) as they need non uniform electromagnetic field distribution because they exhibit zero net dipole with plane wave exposure. If Gans theory is applied to nanorods it can be seen that the increase in aspect ratio (while the diameter being constant) leads to increase in extinction cross section of both

longitudinal and transverse modes fig4 (a) and fig4 (b). A shift in peak position is also observed for both modes but it is more pronounced for longitudinal mode. The
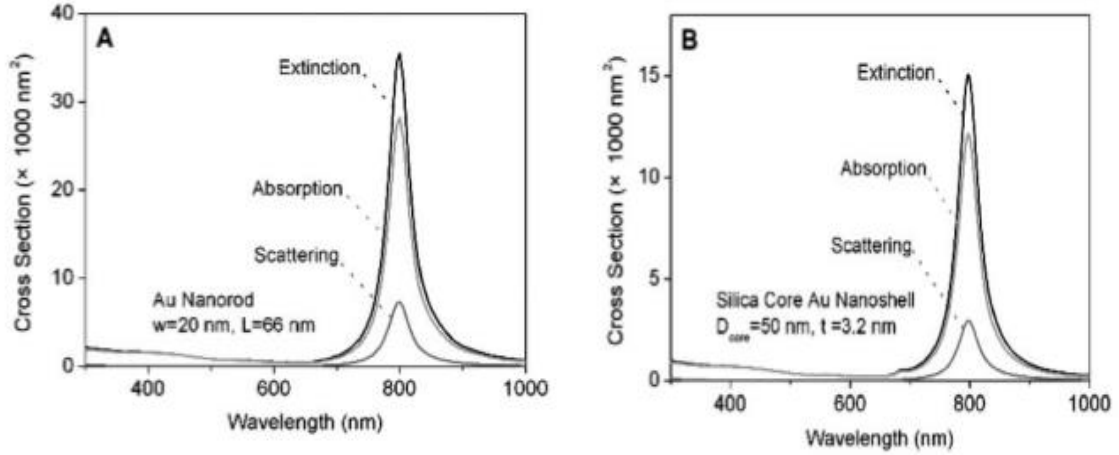
Figure 3. The DDA estimated extinction curves for (A) Au nanorod L=66nm and W=20 nm (B) Si cored Au nanoshells (core dia=50nm and shell thickness =3.2nm)

reason for the larger shift in peak position for longitudinal mode is that the nanostructures with higher polarizabilities (longitudinal mode) induce more polarization charges and hence cause larger shift in peak position. The Gans theory predictions are different than FDTD simulation results as the retardation effect is not considered in Gans theory calculations. As seen in Fig 4 (d) and (e) the enhancement is seen largely in the regions with higher curvature (i.e. at the ends of the rods) because they have higher volume densities of electrons as compared to other regions. The refractive index of the medium also causes the peak to shift. Increase in refractive index of the medium causes red shift. Also, the longitudinal Plasmon shift is linearly related to the rise in refractive index of the

medium [31]. But in this study we have used water as the surrounding medium to all the particles so this factor is irrelevant in our case.
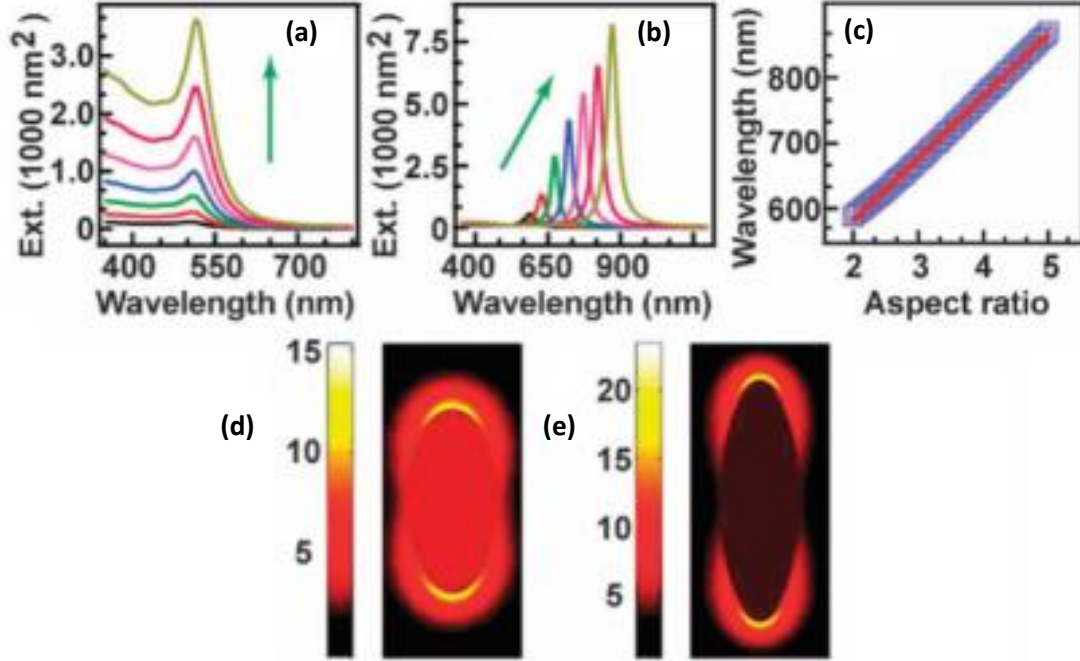
Figure 4. (a) Extinction variation with aspect ratio for transverse mode (b) extinction variation with aspect ratio for longitudinal mode (c) extinction peak wavelength variation with aspect ratio for longitudinal mode (d) electric field enhancement contour (aspect ratio=2) (e) Electric field enhancement contour (aspect ratio=3).

If 2 rods are placed in proximity of each other without actually touching each other, their plasmon resonances will interact with each other electrostatically to form a different collective plasmon mode which is termed as coupling effect. The coupling causes extremely large electric field enhancements and distinct collective plasmon modes. When the rods are aligned end to end the peak position shifts to

the red side and if they are aligned side by side the peak position shifts to the blue side of the wavelength spectrum [32].
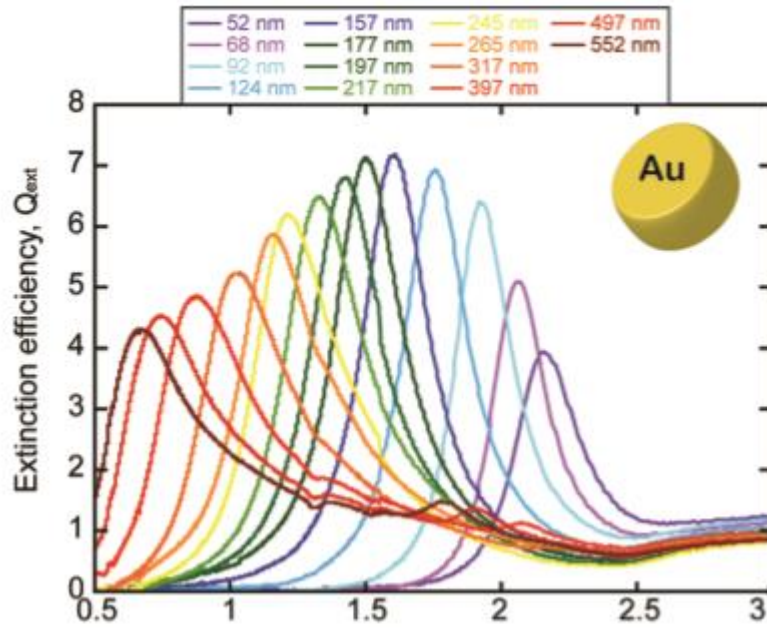
Figure 5. SPR extinction variation vs energy of light source with change in diameter of Au discs (20 nm thick) placed at least 6 times their dia apart from each other [33].

Also, the nanoparticles exhibit damping which limit the coherent lifetime and hence quality factor of local field enhancement of plasmonic oscillations [33]. There are two types of damping: radiative and non-radiative. Both of them are present in case of particles larger than 20-30 nm. The absolute value of damping is dependent on both particle size and the type of material of particles. Radiation damping represents the energy lost by photon emission and it is found to increase with increase in particle size in general. Non-radiative damping represents both intraband (scattering) and interband excitations of electrons (formation of electron

14

hole pair which cascade into multiple pairs later on). Thus damping generates heat and cause the loss of absorbed energy.

In a study a 2D array of 20 nm thick Au discs, which were placed at a distance more than 6 times their diameter apart from each other, was analyzed for absorption. The diameter was varied for every other measurement. The results showed that the peak shifted to lower energy side (i.e red side or higher wavelength of source) of the spectrum with increase in diameter [33] i.e. Fig (5). Here, the coupling effect was kept at minimum as they were placed far apart from each other. The Discs, being arranged like a 2 D structure, have only one mode of plasmonic oscillations. The electron cloud oscillations here are parallel to the face of the disc (i.e. along the disc diameter) [34] whose thickness was 7nm and diameter was 46.5 nm.

2.1.1 FDTD SIMULATION

The numerical computational techniques can be used to determine the solution to Maxwell's equations with irregular geometries and boundary conditions. When it is used to determine the interaction between an electromagnetic field, the physical object and its medium, it is denoted as CEM (Computational electromagnetics). The CEM simplifies the real world structures by approximating the calculation nearest to the idealized structures like cylinders, spheres etc. Besides, it also simplifies the real world structures by using symmetry and reduced dimensionality (like from 3D to 2D to even 1D sometimes). The space considered under calculation is discretized as orthogonal and non-orthogonal grids. Then the Maxwell's equations are solved for each point in the grid. Solving Maxwell's

equations this way needs a lot of computing power and memory and thus it also takes long time. The techniques for solving Maxwell's equations can be divided into two major methods which is either integral equation solver or differential equation solver. The boundary element method (BEM) is an example for integral equation solver which accounts for only the boundary values of the mesh considered under calculation. This technique is more efficient for small surface / volume ratio considerations. But, if the grid volume under consideration is considerably large, then it's better to employ finite element method or FDTD. They are especially better for objects with curved surface geometries. FDTD finds the approximate solutions to Maxwell's partial differential equations. At first, using central difference approximations the time dependent Maxwell's equations are discretized in space and time to partial derivatives. These partial derivatives are then solved in cyclic manner. In the software for a specific volume the electric field vector components are calculated first at a particular instant of time and then the magnetic field vectors are calculated for the very next instant of time for the same space of volume. This procedure is repeated until the steady state EM field behavior that was desired is fully evolved.

FDTD is a better choice as it can cover a wide range of frequencies in a single simulation using Fourier transformation. The wide variety of EM material properties can be treated here. Both for the time domain and for the frequency domain are offered for the unique insights into the problem of an application.

To simplify, we can say that the propagation and interaction of an electromagnetic wave with nanoparticles made of dielectric materials like Au can

be determined by finite differential time domain calculation (FDTD) method. This is done by solving the Maxwell's equations by using both time and frequency domain of the electromagnetic wave under consideration. The area under consideration for calculation is discretized in terms of space and time. The area under consideration is discretized into various Yee cells with the electric and magnetic field unit vectors of the electromagnetic wave along the edges and perpendicular to the face of the Yee cell cube respectively (Fig 7).
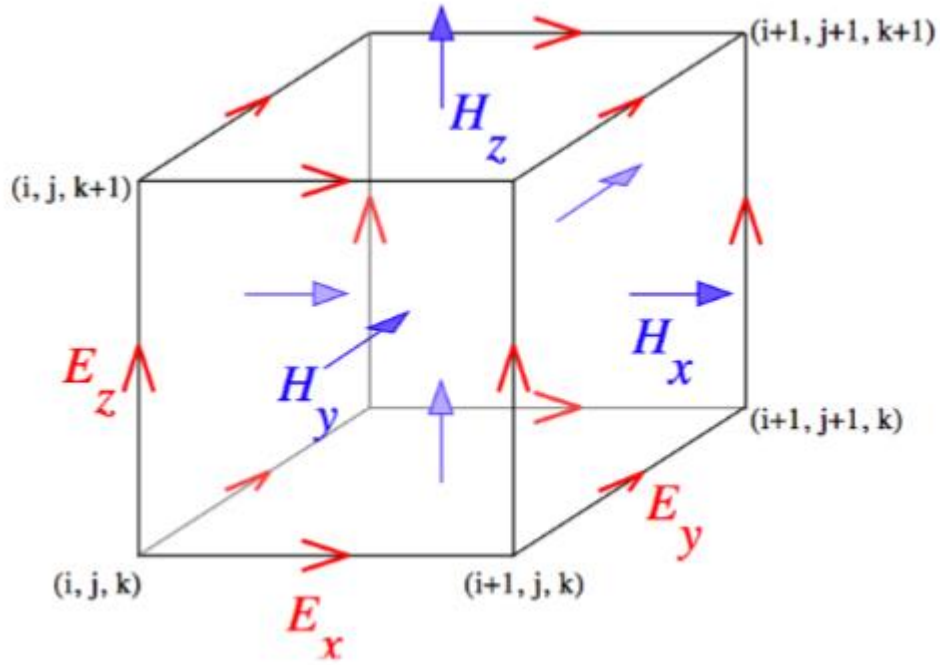
Figure 6. Schematic of a Yee cell

The Schematic of the setup of the simulation can be seen in Fig 8. The different boxes represent different perfectly matched layers (PMLs). The source is placed between the absorbed power monitor and the scattered power monitor. The time monitor is placed inside the absorbed power monitor region. The particle is

surrounded by the water around it on the outside. The polarization of the source's E field is shown by black arrow in the schematics of the setup and direction of propagation of the source is shown by red arrow. The extinction cross section is the sum of absorption cross section and scattering cross section. The refractive index and extinction coefficient were taken from the Johnson and Christy website.
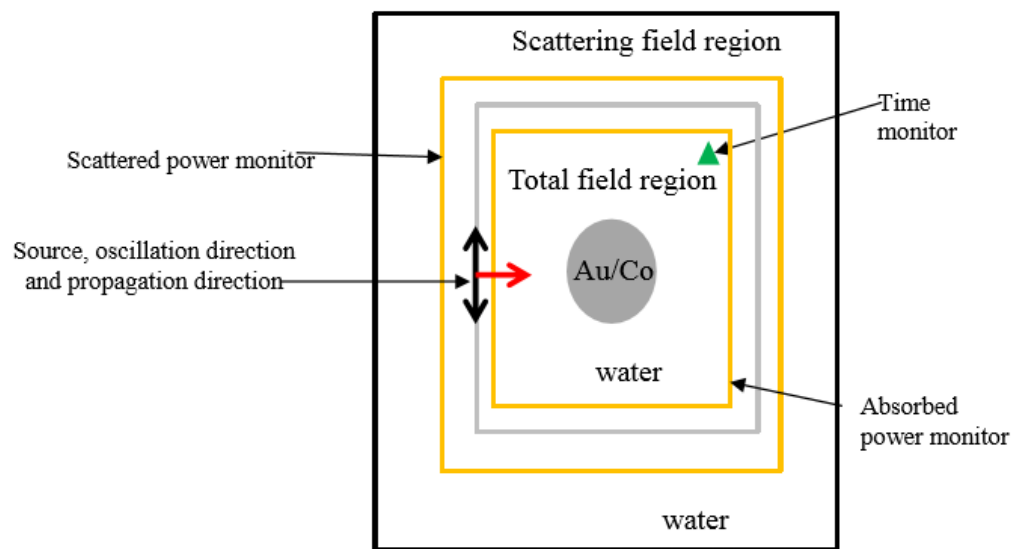
Figure 7. The schematic drawing of the FDTD simulation setup.

The steps for carrying the simulation in the commercial FDTD software can be named sequentially as creating the physical structures, setting the simulation

region and time, defining sources, defining monitors and then finally running the simulation and plotting the results and graphs.

2.2   MAGNETIC PROPERTIES OF MAGNETIC NANOPARTICLES

The balance between various types of energies influences the state of a magnetic material. These energies are mentioned below,

Thermal energy:

Temperature has an important effect on the magnetic properties of nanoparticles. It randomizes the magnetization direction of single domain particles and thus destroys the alignment of magnetic dipoles.

Exchange energy:

This energy is the result of interaction between the magnetic dipoles within a domain of ferromagnetic, ferromagnetic and antiferromagnetic materials. Its value is the lowest when all the magnetizations of all the dipoles in a domain are aligned in the same direction. In case of the regions near the domain walls the magnetizations are obviously in different directions and so the exchange energy is higher in these regions which is proportional to the total area of the domain walls.

Magnetostatic energy:

Magnetic materials which have free surfaces have a demagnetizing field (opposing field, H_d) inside them. The energy associated with this demagnetizing field is dependent on the volume occupied by the magnetic field lines outside the

domain. This energy can be kept in check by limiting the lengths of the loops of magnetic field lines outside the domain. This can be achieved by having multiple domains. So the permanent magnets tend to break domains into smaller domains. This energy depends on the shape of the domain which can be related to N_d (demagnetization factor) and can be calculated by equation (5).

$$E_{ms} = \frac{1}{2}H_d M = \frac{1}{2}N_d M M = \frac{1}{2}N_d M^2 \qquad (5)$$

Here,

H_d is the demagnetizing field

N_d is the demagnetizing factor

M is the magnetisation

Zeeman energy (magnetic potential energy):

This type of energy can be seen in a magnetic material that is exposed to an external magnetic field. This energy can be added or subtracted to magnetostatic energy as they both are kind of similar to each other. If the domain magnetization is arranged parallel to external applied magnetic field the Zeeman energy decreases and if it is arranged opposite to the external field then the Zeeman energy increases. The Zeeman energy is proportional to negative cosine of angle between the magnetization and direction of external applied magnetic field. So when the ferromagnetic material is magnetized by using external magnetic field, the domain walls move so that the domains with magnetization parallel to the external field increase in volume and the ones opposing the external

field decrease in volume. If the external applied field is strong enough then all the domains that possess magnetization opposite to the field will vanish and the magnetization of the material can then be denoted as saturation magnetization beyond that applied field value.

Crystal anisotropy energy:

The energy of a magnetic material associated with its tendency to align its magnetization to a preferential crystallographic direction is termed as magneto crystalline anisotropy or crystal anisotropy energy. The uniaxial anisotropy energy density is given by equation (6). HCP Co has uniaxial anisotropy. For cubic system it is given by equation (7). FCC Ni and BCC Fe have cubic anisotropy.

$$E_{ani} = K_{u1} \sin^2 \theta + K_{u2} \sin^4 \theta \qquad (6)$$

$$E_{ani} = K_1 \alpha_1^2 \alpha_2^2 + \alpha_2^2 \alpha_3^2 + \alpha_3^2 \alpha_1^2) + K_2 (\alpha_1^2 \alpha_2^2 \alpha_3^2) \qquad (7)$$

Here,

θ is the angle between magnetization and easy axis

K_{u1}, K_{u2}, K_1, K_2 are the anisotropy constants.

α_1, α_2, α_3 are the projections of unit vector on 3 crystalline easy axis.

Shape anisotropy:

A spherical nanoparticle, with no total crystalline anisotropy, will have same magnetization in any direction when under an influence of external applied field. Whereas, a non-spherical specimen, with no total crystalline anisotropy, will have a total magnetization in its elongated axis direction in order to reduce the

21

magnetostriction energy (magnetostriction is the property of a ferromagnetic material that helps them to change their shape or dimensions).

In general an ellipsoid has three axes (a, b, c) and the demagnetizing factors are N_a, N_b, N_c, such that $N_a + N_b + N_c = 4\pi$. The shape anisotropy energy is the lowest in the direction of the smallest demagnetization factor which is termed as the easy axis.

Size effect:

Domain is a region in which all the magnetic moments are pointed in the same direction. Domains are separated from each other by domain walls. Multiple domains are usually seen in bulk materials as it helps to reduce the overall energy of the material. The exchange energy, magnetostatic energy and anisotropy energy all together decide the shape and size of the domains in a material. The thickness of the wall is decided by balancing of exchange energy and anisotropy energy, as they kind of counteract each other in this aspect to minimize the total energy.

As we reduce the size of the particles, the particle changes from multi domain to single domain to superparamagnetic. As the particle volume is decreased the size of the domain is decreased. As the domain size goes down the domain wall energy keeps on increasing but magneticstatic energy keeps it in check and keeps the total energy down by reducing itself. But after certain limit when we still decrease the size of the domains, the magnetostatic energy can no longer contain domain wall energy and the particle can't break into domains

anymore and becomes a single domain particle. The critical diameter for spherical particles so that they become a single domain particles depends on saturation magnetization, anisotropy and exchange energy which can be seen in equation (8).

$$D_c = 18\sqrt{AK_a}/(\mu_0 M^2) \qquad (8)$$

Here,

A is the exchange constant

K_a is anisotropy constant

M saturation magnetization

μ_o is vacuum permeability

Superparamagnetic particles possess high susceptibility and little or no remanence. This helps them to reach higher magnetization values at relatively lower applied external field and don't let them to get aggregated after the external field is removed. In superparamagnetic particles the volume of particles is proportional to anisotropy energy. When the particle size gets small enough the temperature can easily flip the magnetization direction of the particle and thus it then has zero remanence. The energy curve for superparamagnetic particles is given in Fig (6). So the superparamagnetic particles are desirable for biomedical applications as during the treatment the particles are expected not to agglomerate and reach saturation at very low external fields. The flipping frequency of the

direction of the magnetization can be determined by Arrhenius equation [equation (9)].

$$r = \mathcal{f}_0 e^{-\frac{\Delta E}{kT}}$$ (9)

Here,

$\mathcal{F}_0$ is thermal attempting frequency

ΔE is the Energy barrier

k is Boltzmann constant

T is the temperature
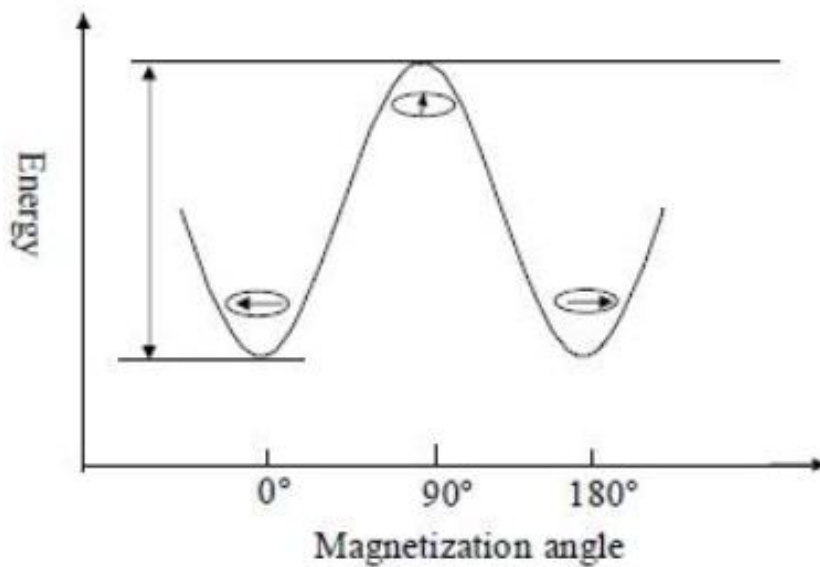
Figure 8. Energy Vs magnetization angle for superparamagnetic particles.

The particle size has huge effect on the hysteresis loop as well. If the multi domain particles have large domains the hysteresis loop is narrow as smaller field is enough for the shifting of its domain walls. If the multi domain particles have

24

small domains the hysteresis loop is broader because it has to rotate large number of domains and move large number of domain walls which needs a larger field before it get saturated. But since superparamagnetic particle's moment is free to fluctuate and have ordered structure they don't show hysteresis loop and instead show sigmoidal magnetization Vs applied field curve which has no remanence and no coercivity.

3 FABRICATION

The fabrication of multilayered nanoparticles in this study include a series of steps. First, the AAO template with ~ 100nm channels is produced by the anodization of the metal aluminum foils at high potential (>40V). Then different metal layers were deposited in the channels of theses templates by electrodeposition. And finally, these particles were released into water suspension by dissolving the AAO membrane.

3.1 SYNTHESIS OF ANODIC ALUMINUM OXIDE (AAO) MEMBRANE TEMPLATES

Anodic Aluminum Oxide (AAO) are chosen for multilayered nanoparticle synthesis because using them as templates is easier and cheaper when compared to nanoparticles made by other technique such as photolithography. The channel diameter of AAO can be controlled by changing the anodization potential, pH and etching temperature or the etchant itself [35].

The anodization was conducted in an electrochemical cell with the aluminum foil as anode and oxalic acid as electrolyte. The anodization setup consisted of a two electrode cell (Fig. 9). The aluminum foil that was to be converted to a porous alumina membrane was made as an anode and a Pt mesh was used as cathode. They were hooked up to a DC power supply (which was controlled by a computer with Labview software). The two electrodes faced each other and were 2.5" apart from each other. To maintain the uniformity of the current density on all over the exposed surface of Al foil, the foil was placed directly on top of (thus directly in contact with) Cu plate attached to a Cu rod at its base. Also the

Pt mesh is placed in such a way that it cover the entire exposed surface of Al foil. The hydrogen bubbles that evolve at cathode during the anodization tend to agglomerate and form huge bubbles in the cell and so the mechanical stirrer was employed to continuously stir the electrolyte and expedite the bubble outing. The anodization process is conducted with 40V potential; a high current passing through electrolyte, generating significant amount of heat. To lower the electrolyte temperature, the setup was placed inside a refrigerator (around 4^0c) throughout the anodization.

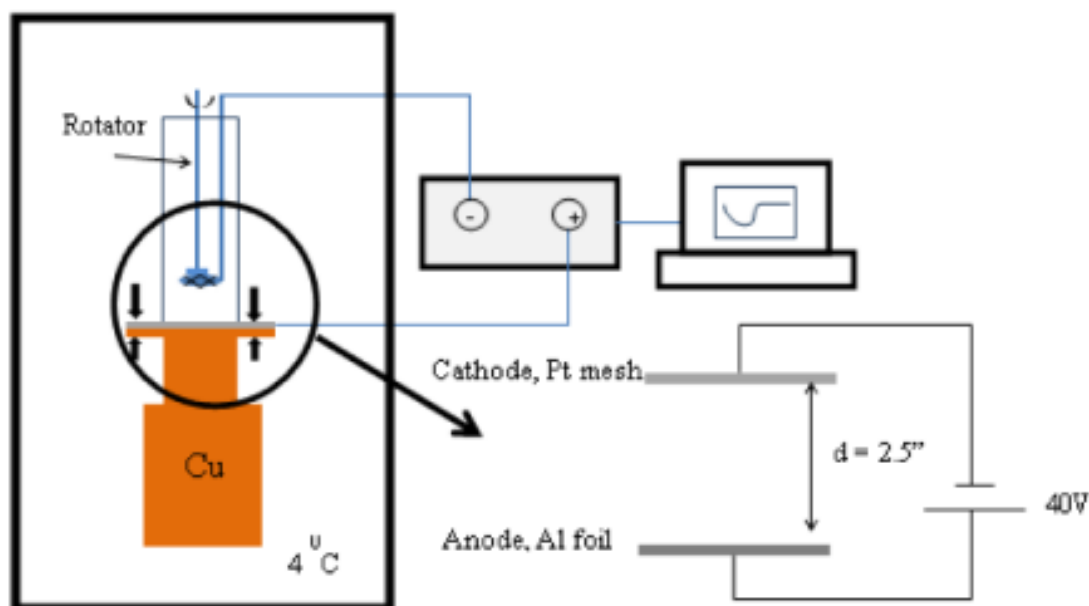Figure 9. Sample schematics of Anodization setup

The rolled Al foil (from Alfa Aesar) used for anodization was 99.45% pure and was cut into 2x2 cm^2 size. The Al piece was then placed on a Cu plate (which was attached to the blocky cu base beneath for better heat transfer) and taped to the plate by a conductive Cu tape on the side. Then a glass vessel, which was

open at both ends, was placed on top of Al foil with a rubber O ring placed in between the glass vessel and the Al foil to make a sealed cell. The cell was clamped to the Cu plate by a large clamp which could be tightened by screws on it. The exposed area of Al foil to electrolyte was 1.776 cm^2. The foil was then cleaned with acetone and ethanol (one after another) to remove any grease or impurities on the surface of the foil, followed by rinsing with deionized water a few times. Then 0.23 M oxalic acid solution was poured into the assembly cell and the assembly was later kept in the freezer to cool down for about 10 mins. This initial cooling would make sure that the assembly is not at room temperature when the anodization starts. This is necessary because the temperature rises very quickly when anodization begins whereas cooling down by heat transfer is relatively slower process. The cell assembly was then connected to a DC power supply which is controlled by LabVIEW software on a computer and anodization was done at 40 V for 6 hrs at 4^0C. Once the anodization was done the Al foil was converted to porous alumina with channeled structures (Fig. 10).
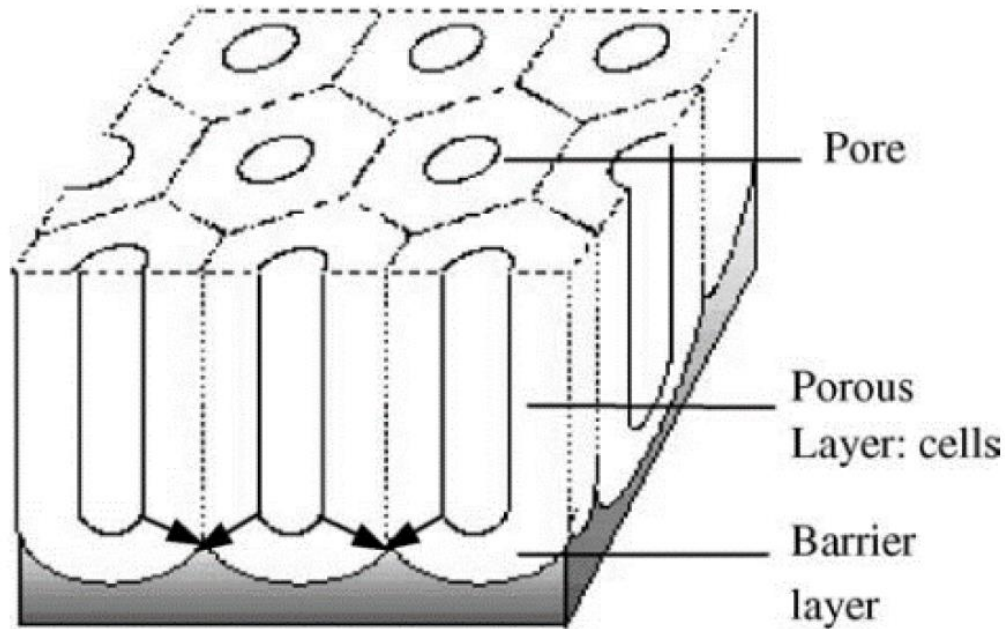
Figure 10. AAO right after anodization with unopened pores at the bottom.

To better understand the anodization process, we can divide it in a few phases (Fig. 11). Initially when the anodization is started, the current is very high which drops to a very small value in just a few seconds. This is a result of formation of a continuous Al oxide film on the top of the exposed Al film surface. This film grows for a few more seconds and the current is still lower during this phase (phase a in Fig. 11). Later on, the film breaks at certain places and it forms number of dimples on its surface (phase b). The current still continues to drop in this phase. Even though the pore are progressing towards bottom they haven't reached to the Al interface yet. Once they reach the metal interface the current starts to rise (phase c). The conductivity of the foil increases and so the current can be seen increasing during this phase. By the end of phase c the rate of progression of the pores is stabilized and so the current density also stabilizes to more or less a

constant value. The phase with the constant current density is the last phase of AAO porous structure formation (phase d). The current is stable during this phase because the pores keep on progressing towards the bottom at about the same rate throughout this phase. There is an oxide to metal interface towards bottom and an oxide to electrolyte interface on top where oxide is exposed to oxalic acid. In this phase the oxide layer keeps on dissolving in the oxalic acid and new oxide keeps on forming at the metal to oxide interface during anodization. Thus, the oxide layer progresses towards the bottom of Al foil. These two rates, oxide layer formation and oxide layer dissolution, balance each other and thus maintain a steady rate of pore propagation.
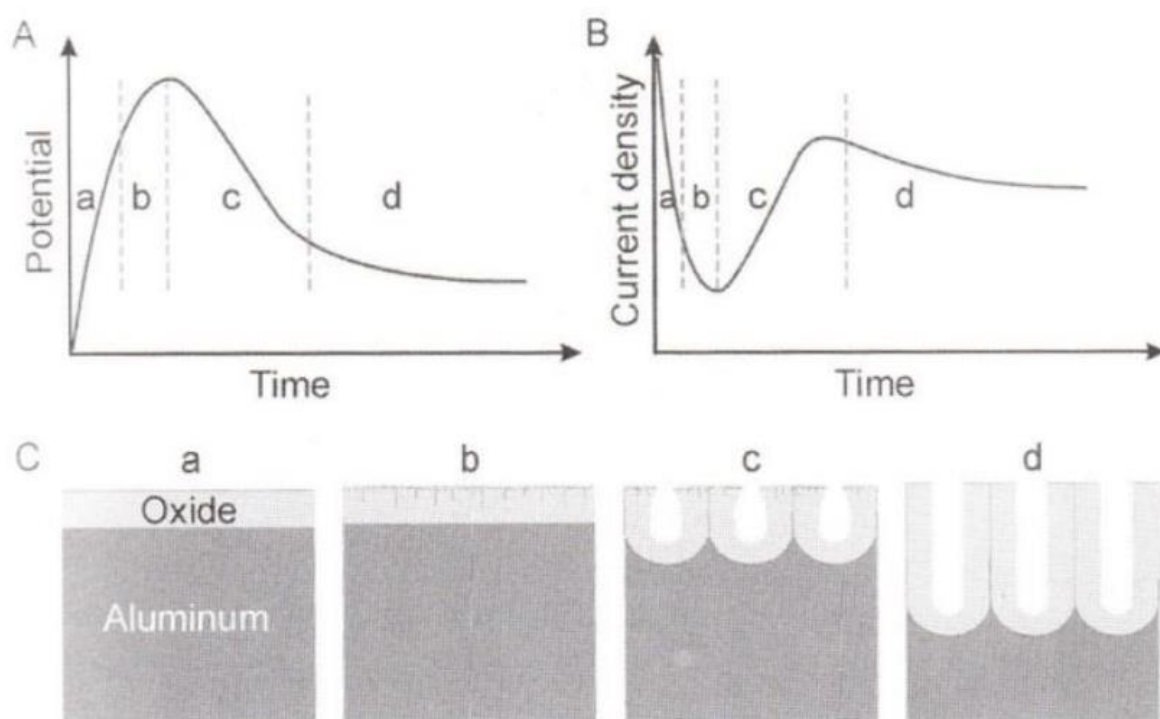

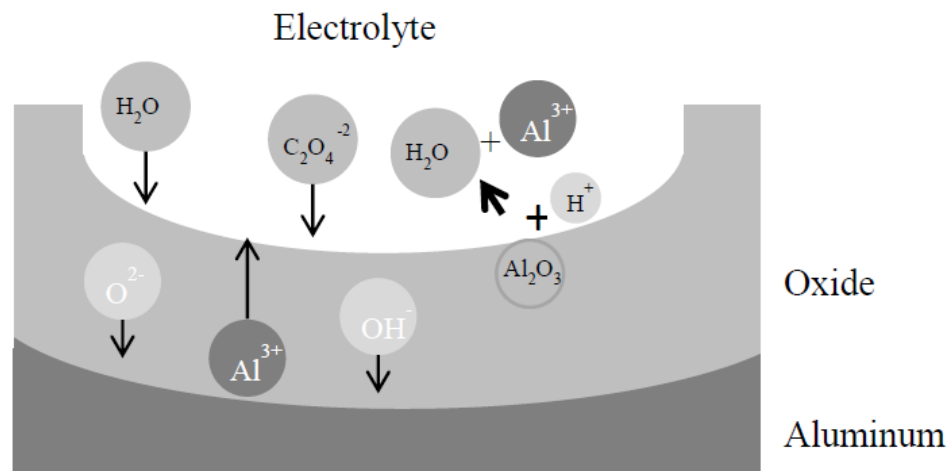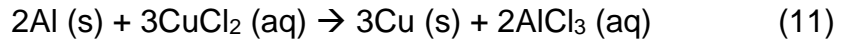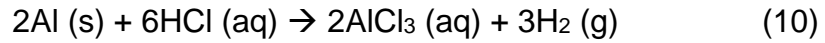Figure 11. Phases of anodization (Pore formation and progression) [36]

Figure 12. The ion exchanges during pore progression into the Al foil.

The electrolyte contains oxalate ions ($C_2O_4^{2-}$) (Fig. 12). With these ions being negatively charged and aluminum being anode (+ve electrode) the oxalate ions penetrate into the oxide and travel towards the anodic aluminum. Before oxalate ions reach the bottom they form $Al_2(C_2O_4)_3$. It is found that $Al_2(C_2O_4)_3$ is less dense than alumina and it was found more in concentration only at the bottom of the pores and very less in the channel walls [37]. The important thing to mention here is that this migration of oxalate ions is irrelevant to the Al oxide formation and dissolution that is going on there as well simultaneously. The progression of pores towards the bottom in the Al foil happens due to the applied electric field. The electric field, E, get stronger with the decrease in thickness of the foil (d). This can be seen from $E = V / d$. In our case the external potential is maintained constant at 40 V and the d value is lower in the bottom of the channels than other locations in the top. So E is very strong at the bottom of the channels which helps dissolution of alumina there. Thus, it is believed that the bottom oxide layer dissolves more than the wall oxide and thus pore continue to dissolve in downward direction.

Still, the work is not done yet as the channels are not open on the bottom side of the foil and also there is some Al left at the bottom. So, in order to make AAO ready for use, the bottom Al layer and the alumina barrier layer (U shaped Alumina wall at the bottom) have to be removed. This is done by using a solution consisting of 0.24M $CuCl_2$ (40g/L) and 40ml of concentrated HCl for 1 liter of DI water. The reactions for Al dissolution are mentioned in equation (10) and equation (11). This process usually took 5 to 10 mins.

$$2Al \text{ (s)} + 6HCl \text{ (aq)} \rightarrow 2AlCl_3 \text{ (aq)} + 3H_2 \text{ (g)} \qquad (10)$$

$$2Al \text{ (s)} + 3CuCl_2 \text{ (aq)} \rightarrow 3Cu \text{ (s)} + 2AlCl_3 \text{ (aq)} \qquad (11)$$

Then later, 1.16 M phosphoric acid was used to open up the pores i.e. (to dissolve the bottom U shaped Alumina layer). This takes about 80 mins. This process can also be used for widening the pores of the membranes. We used 80nm channel diameters for the experiments which took 80 mins. Longer time would be needed for larger diameter of channels. The reactions for pore opening are shown in equation (12).

$$Al_2O_3 \text{ (s)} + 2H_3PO_4 \text{ (aq)} \rightarrow 2AlPO_4 + 3H_2O \text{ (l)} \qquad (12)$$

It was seen that the pores widen both on the top and the bottom side of the membrane during the phosphoric acid mediated pore opening procedure (Fig. 13 and Fig. 14). It was also seen that if the pore opening was continued for 100 mins or more, the membranes were completely dissolved. The total thickness of the membranes was around 10 μm. The template was washed and soaked in DI water overnight before drying to clean its pores of all the previously used chemicals. And

finally, the template was coated with Cu on the bottom side of the membrane by thermal evaporation to make working electrodes for subsequent electrodeposition.
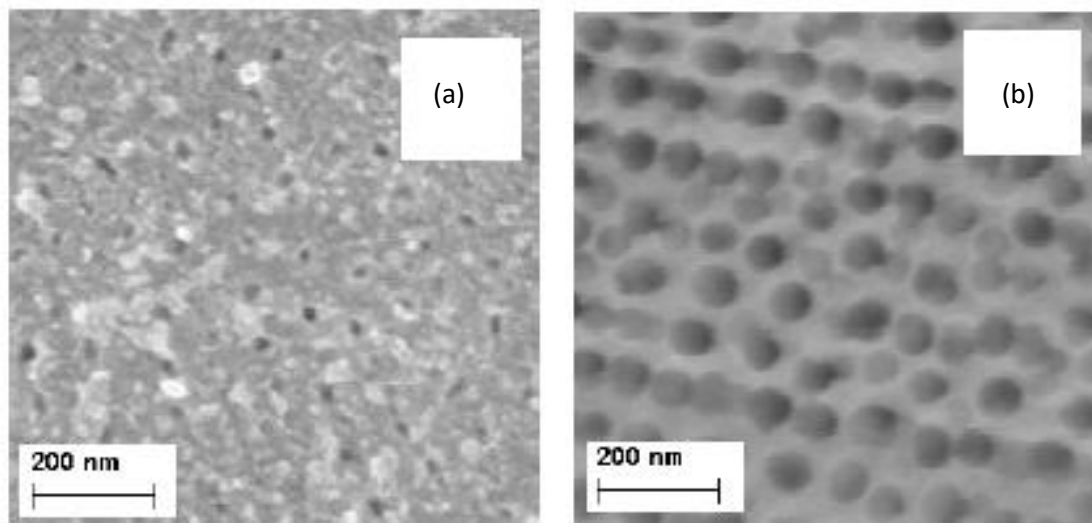

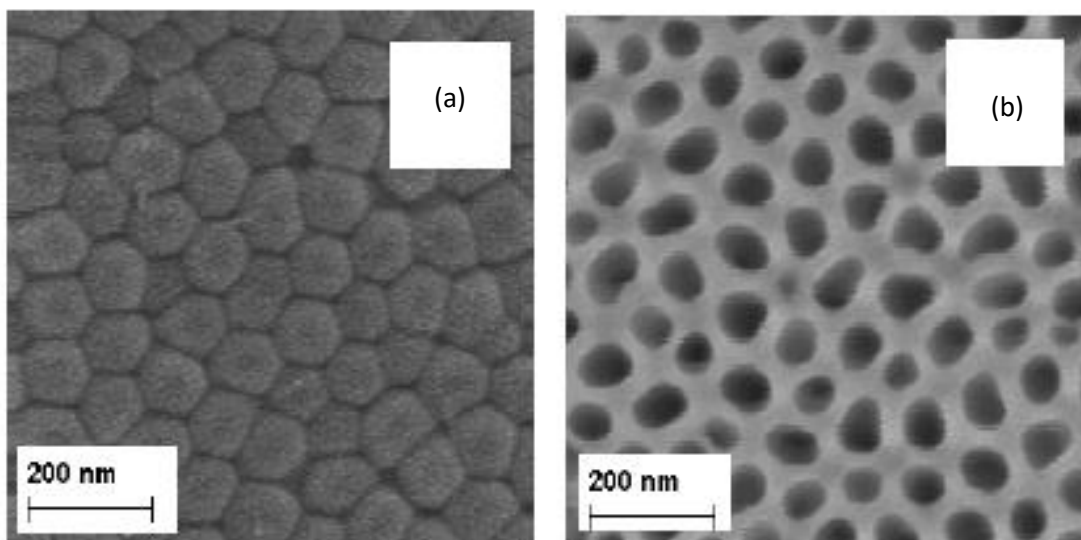Figure 13. SEM of the top surface (a) before pore opening and (b) after pore opening for 80 mins

Figure 14. SEM of bottom side of the AAO template (a) before pore opening (b) after pore opening of 80 mins

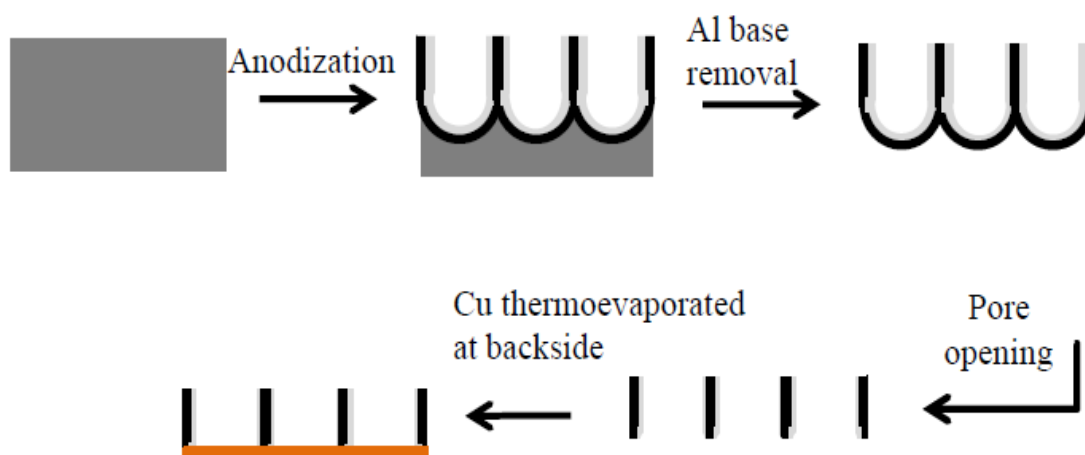The entire template synthesis procedure from Al foil to the ready template is summarized in Fig. 15.

Figure 15. Summary of AAO template making

The porosity of the membranes is termed as the ratio of surface area containing pores to the total surface area of the membrane under observation. Using simple geometrical calculations, the porosity can be calculated by using the equation (13). For this calculation it is assumed that the individual cell in the membrane is hexagonal and the pore in its center is circular pore hole. Using this equation its can be estimated that after 80 mins of pore widening the porosity of the bottom surface of the membrane is 0.54 (by estimating pore diameter to be 88 nm). So, roughly 50 % of the total area of the membrane is porous after 80 mins.

$$\alpha = \text{area of pore} \, / \, \text{area of hexagonal cell}$$

$$\alpha = (\pi \, D_p{}^2 \, / \, 4) \, / \, (3\sqrt{3} \, D_c{}^2 \, / \, (2\sqrt{3})^2)$$

$$\alpha = \ 0.907 \left(\frac{D_p}{D_c}\right)^2 \tag{13}$$

here,

D_p is the pore diameter

D_c is the cell size (i.e. inter pore distance)

3.2 ELECTRODEPOSITION

350 nm Cu was first coated onto the bottom of the membrane by a thermal evaporation process. The coating rate varied during the evaporation. In the initial stages it was very low and then as the coating progressed the rate was raised to a relatively higher uniform coating rate. The initial 50 nm were coated with the coating

rate of 0.05nm per second which was then raised to 0.1 nm per seconds until the total deposited thickness had reached to 100nm. After 100 nm the coating rate was raised to 0.2 nm per second until the total of 350 nm was deposited onto the membrane. The reason behind varying the rate of deposition was to get the Cu coating bonded to the membrane properly and also to promote some cu coating inside the channel on the bottom end of the template. This helps the electrodeposition of Cu to be carried out later on.

Even though the membranes were thermal evaporation coated with Cu on the bottom side of the membrane, this coating can't still cover up the channels completely and so if the electrolyte is poured into them it can easily leak out from the bottom. So in order to close these gaps and also in order to make a flat base for subsequent nanoparticle deposition, we have to deposit Cu by electrodeposition in the channels. This deposited Cu can be etched away easily later by using Cu etchant and so it is used just for sacrificial purposes here. The pulse electrodeposition method was employed for the synthesis of the nanoparticles in the AAO templates. The single bath electrolyte containing both Au and Co was used for the electrodeposition. This method is cost efficient for synthesis of large number of particles. The 3 electrode cell was used for electrodeposition. The Membranes with evaporation deposited Cu served as the working electrode. The Ag/AgCl in saturated KCl solution served as the reference electrode, and the Pt mesh served as the counter electrode which possibly facilitated O_2 evolution. Cu was electrodeposited into the channels with total charge of 8C, which corresponds to 4-5 µm thickness of Cu. The electrolyte used for Cu

deposition was composed of 0.5 M Cu sulfate, 10 ml of sulfuric acid per liter of DI

water (table 1). The assembly of 3 electrode cell is shown in Fig. 16. There it can

be seen that the Cu coated membrane (i.e. working electrode) goes at the bottom

of the 3 electrode cell. It is attached to a Cu plate with a Cu tape so that the

conductivity can be maintained and that it can be connected to the potentiostat.

The evaporation coated Cu layer goes to the bottom of the assembly so that the

channels in the template are exposed to the electrolyte which can then enter the

channels.

Electrolyte	Compositions	
	$CuSO_4.5H_2O$	0.5 M
Cu	H_2SO_4	0.5 M
	DI water	100 ml

Table 1. The electrolyte composition for Cu electrodeposition

The electrolyte was poured into the cell usually about 30 mins before

electrodeposition started, allowing electrolyte to fill up the channels and squeeze

out the air bubbles inside channels. The Cu deposition was done in 2 steps. First,

a higher potential (-0.1 V vs Ag/AgCl electrode) was used, and deposited a total of

4 C. Then, a lower potential (-0.005V vs Ag/AgCl electrode) was used for another

total charge of 4C. The reason for doing the Cu deposition in 2 steps was that the

higher potential is needed to start the electrodeposition, which can be attributed to

the existence of oxide on the Cu electrode surface (if the Cu deposition was done

with only lower potential it was sometimes found that the Cu deposition occurred

only on the already thermally deposited Cu and not inside the channels). The

applied potential was lower than the equilibrium potential of the Cu reduction reaction. We can verify this as given below,

Cu^{++} + 2e$^-$ → Cu   e^0 = 0.342 V (standard Cu reduction potential)

But the actual molarity of the Cu electrolyte used was 0.5 M. So we can calculate the equilibrium potential by using nernst equation as,

$$e = e^0 + \frac{0.059}{2} \log[Cu^{++}] \qquad \text{(At 25}^0\text{C)}$$

$$\therefore \; e \; = \; 0.342 + \frac{0.059}{2} \; log[0.5]$$

$$e = 0.333V$$

The equilibrium potential for Ag/AgCl electrode is 0.197 vs equilibrium standard hydrogen reduction potential. Thus, the equilibrium potential for Cu reduction (0.333V) is higher than the Ag/AgCl equilibrium potential (0.197V). So potential values lower than Ag/AgCl equilibrium potential were chosen for Cu electrodeposition to make sure the Cu deposition will occur.

After the first layer of Cu was deposited, the higher potential will result in a fast Cu deposition. This fast deposition at higher negative potential helped to close the pores faster. However, this will lead to the poor filling of the channels, lower potential deposition is needed after the initial higher potential deposition to completely fill the channel with Cu.

After the Cu electrodeposition the Cu electrolyte in the cell was thrown out and the template was washed with DI water to clean the channels. The template

was then dried to remove the water from the channels so that the next incoming electrolyte won't get diluted in there that could cause troubles in electrodeposition due to change in the electrolyte composition. Also, a stirring rod was implemented during the electrodeposition so that the ion concentration is homogenous everywhere. The stirring rod also helped the evolution of gases (probably O_2) during the electrodeposition and thus reduced the entrapment of bubbles in the Pt mesh which could bring down the conductivity during electrodeposition.
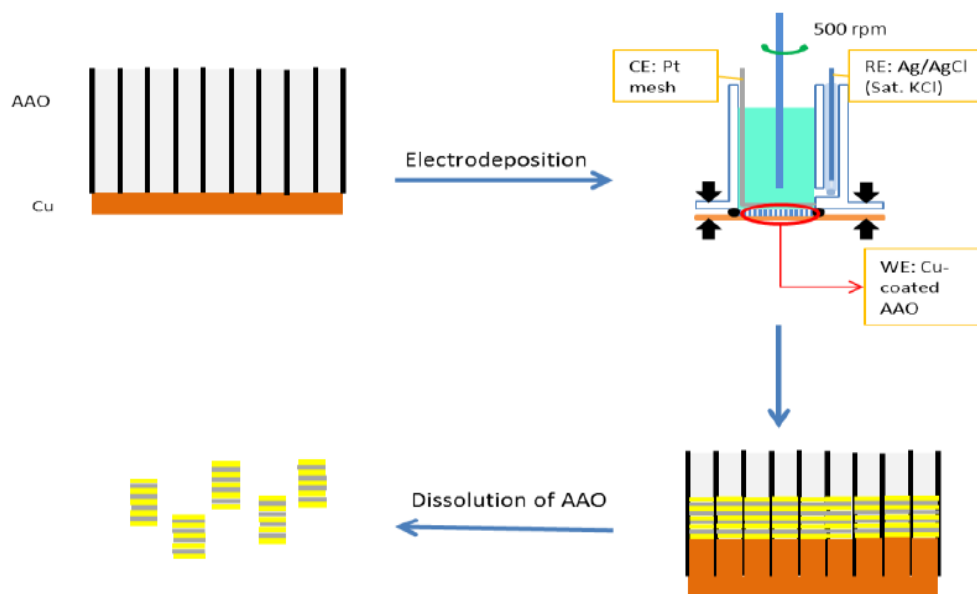

Figure 16. The summary of Au-Co multilayered Nano particle making process.

Next, the Au-Co single bath electrolyte was poured into the cell 30 mins before the electrodepostion to make sure all the air in the channels was let out. After the soaking of the working electrode, the cell was connected to the potentiostat again and the pulse electrodeposition was carried out. The stirring rod was kept on while multilayer electrodeposition was going on. Here, alternate layers of Au and Co were deposited alternately changing the deposition potential. The

number of cycles run (Au and Co layer) was dependent of the number of layers to be deposited in the multilayered particles. The Au layer is present at both ends. For example, if we had to make a total of 9 layers, the Au – Co cycle would be run for 4 cycles and the end deposition would be gold again. Thus making a total of 9 layers. Once the electrodeposition of multilayered particles was done the template membrane was washed with DI water again a couple of times to get rid of the electrolyte in the channels.

To avoid the codeposition of both Au and Co, the electrolyte maintains a huge difference in the ion concentrations of these two metal ions (here [Au] << [Co]). The single electrolyte bath used for this study has 0.285 M Co and 0.3mM Au (Table2). Using the similar calculations, as mentioned before for Cu, the equilibrium potentials for Au and Co were determined as 1.27 V and -0.49V (Vs Ag / AgCl electrode) respectively. The potentials used for Au and Co deposition were -0.7 and -1.1 (Vs Ag / AgCl electrode) respectively which are far below the equilibrium potentials and are well apart from each other. Due to this huge set potential difference the deposition of Au or Co individually should be quite possible in a single bath electrolyte.

Electrolyte	Composition	
	$KAu(CN)_2$	0.3mM
	$CoSO_4.7H_2O$	0.285M
Au - Co	$C_6H_8O_7$	0.8M
	DI water	100ml
	Sat KOH	Adjust pH to 3.5

Table 2. Single bath electrolyte composition for Au and Co multilayer electrodeposition

3.3 TEMPLATE DISSOLUTION AND PARTICLE WASHING

The multilayered particles are still not ready for further use or for characterization right after electrodeposition. To get the particles suspended in water we still have to go through a few more steps. After the template was dissembled from the cell and thoroughly washed, it was subjected to Cu etching. The thermally evaporated Cu and the electrodeposited sacrificial Cu was dissolved in the etchant in just a couple of minutes. The template was then rinsed with water again. Then, the membrane was moved in to a centrifuge tube and 2 M NaOH was added and kept for 20 mins. It was then sonicated for a minute or two to help any leftover membrane (if any) dissolve in NaOH. Then, it was subjected to centrifugation at 7000 rpm for 10 minutes to let the particles to settle down at the bottom of the centrifuge tube. The NaOH was pulled out of the tube leaving the particles at the bottom of the tube. The DI water was added to the tube and the

particles were sonicated for another minute. Later they were centrifuged again at 7000rpm for 10 mins. This water washing and decantation was repeated 2 more times to make sure all the chemicals used until now have been washed away clearly from the particles. Finally DI water was added to the tube and particles were sonicated to get them uniformly suspended in the DI water. The particles are now ready for use or for characterization.

4 RESULTS AND DISCUSSION

4.1 OPTICAL PROPERTIES OF MULTILAYERED NANOROD WATER SUSPENSION

The multilayered nanorod water suspension is measured using UV-Vis spectroscopy. The particles were suspended in water for the measurements. They were sonicated just before the measurements to get rid of any particle agglomeration, if present. The disposable cuvettes, which can accommodate 1.5 to 3 ml of the sample, were used for the measurements.

All the samples displayed a single absorbance peak with the position of peak changed with different types of nanorod. The absolute value of absorbance seen was dependent upon the concentration of particles in the measured sample. More the concentration was, larger was the absorbance peak's absolute value. The concentration of particles wasn't measured and so change in the absolute values of absorbance weren't analyzed in this study.

Five different types of particles were tested for UV Vis absorption spectroscopy (shown in Fig.17 to Fig.22). The diameters of all the multilayered nanorods made in this study were around 80 nm.
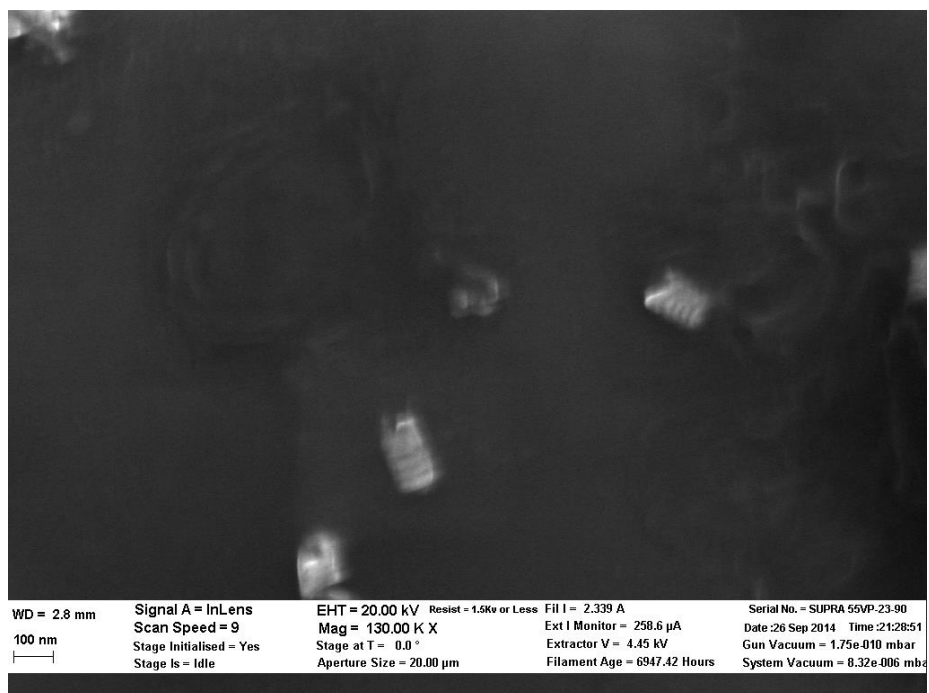
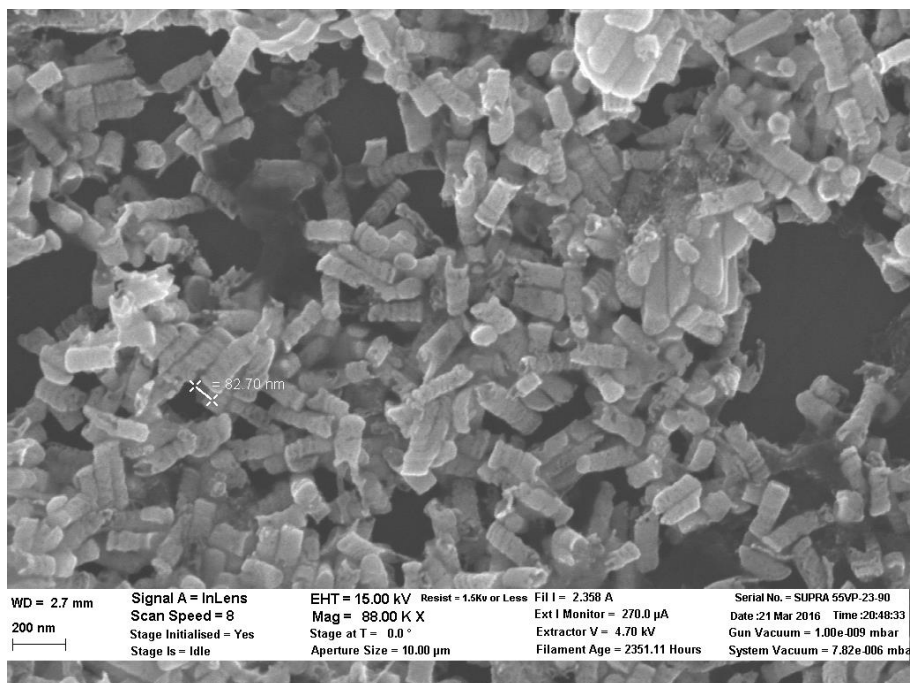Figure 17. SEM image of 9 layered nanorods (short Au and Co).

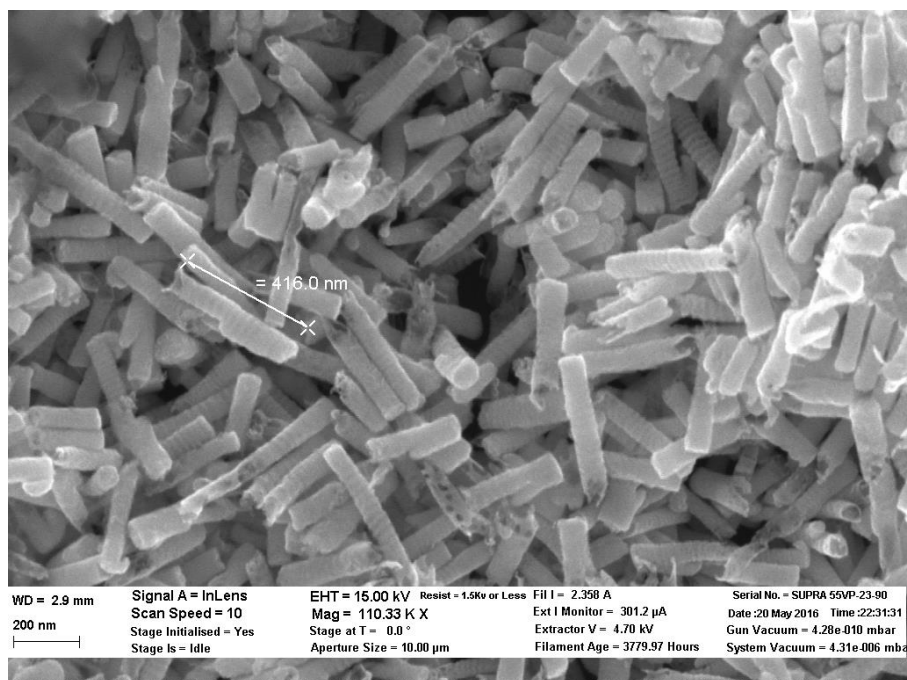Figure 18. SEM image of the 11 layered nanorods (short Au and Co).

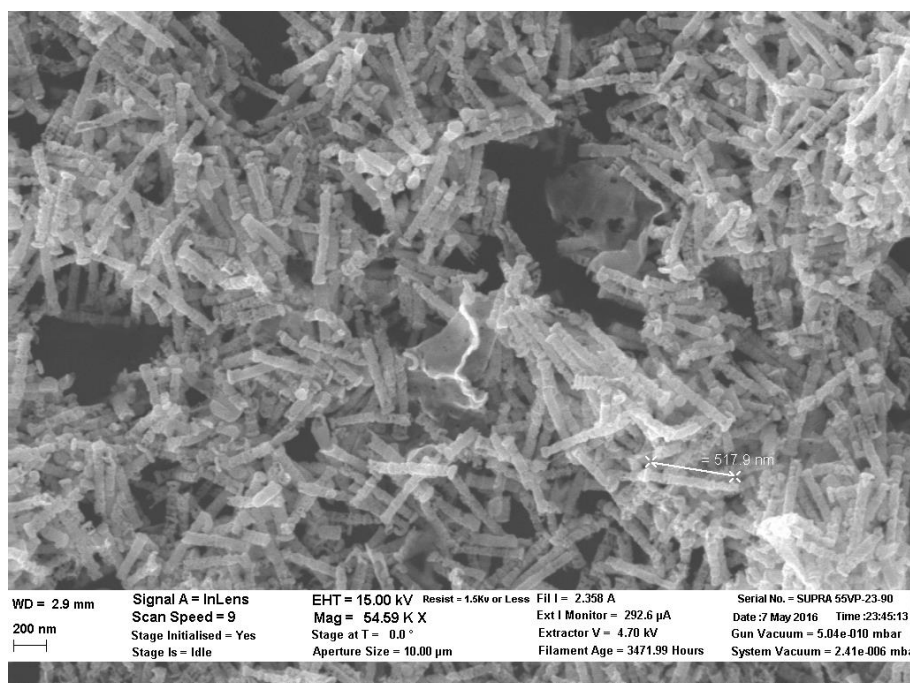Figure 19. SEM image of 31 layered nanorods (short Au and Co).

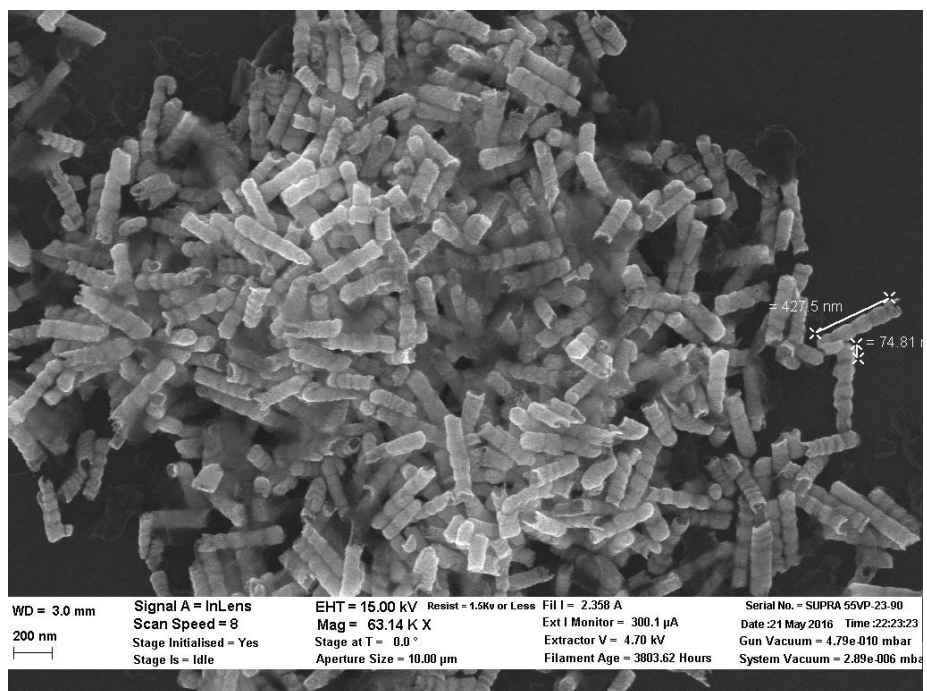Figure 20. SEM image of 9 layered nanorods (short Au and long Co).

= 427.5 nm

= 74.81 nm

WD = 3.0 mm | Signal A = InLens | EHT = 15.00 kV | Resist = 1.5Kv or Less | Fil I = 2.358 A | Serial No. = SUPRA 55VP-23-90
Scan Speed = 8 | Mag = 63.14 K X | | Ext I Monitor = 300.1 µA | Date :21 May 2016 Time :22:23:23
200 nm | Stage Initialised = Yes | Stage at T = 0.0 ° | | Extractor V = 4.70 kV | Gun Vacuum = 4.79e-010 mbar
| Stage Is = Idle | Aperture Size = 10.00 µm | | Filament Age = 3803.62 Hours | System Vacuum = 2.89e-006 mba

Figure 21. SEM image of 9 layered nanorods (long Au and short Co).
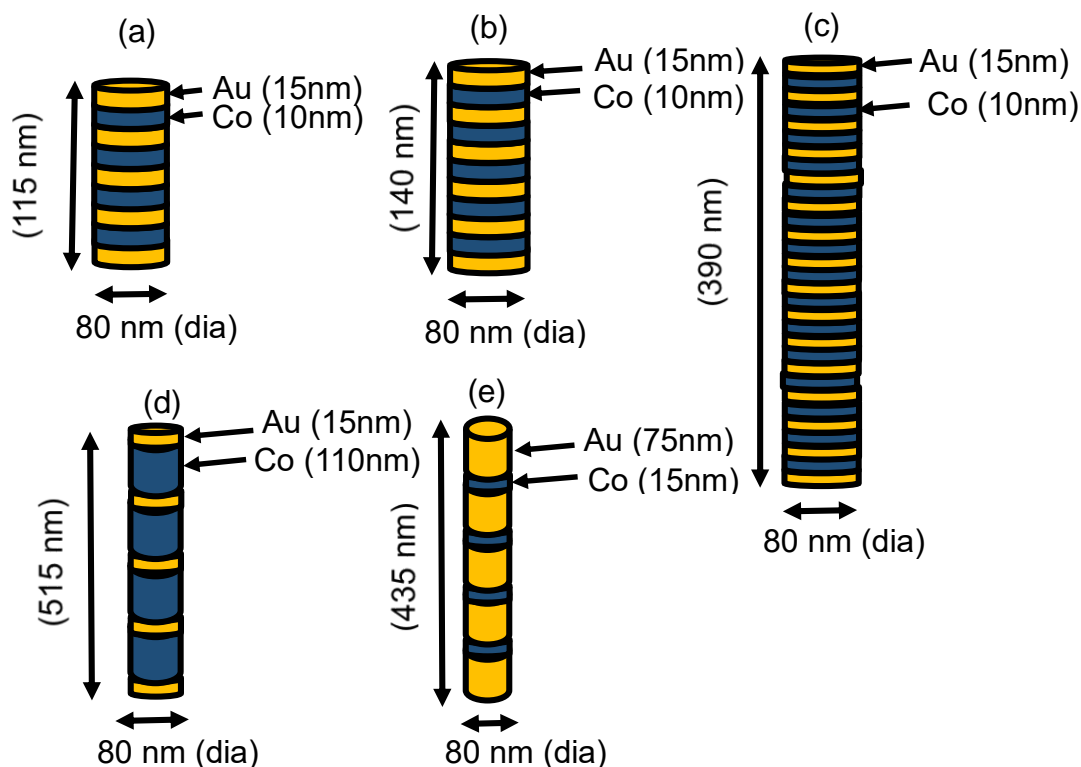
Figure 22. Schematic drawings of the different types of particles under study where (a) to (e) represent Fig.17 to Fig.21 respectively

The peak was observed at around 612 nm (Fig 23) for the multilayered nanorods with 9 layers in total (5Au and 4Co layers). When compared with 11 layered particles the peak appears to be shifted to the blue side of the spectrum (i.e. to the lower wavelength side) by a small amount. The absolute absorbance values are different from that of the 11 layered short sample and this suggests that there is difference in the concentration of the particles in between these two samples. The total length of these 9 layered short multilayered particles is about 120 nm (fig17) and each Au and Co layer is about 15 and 10 nm respectively.
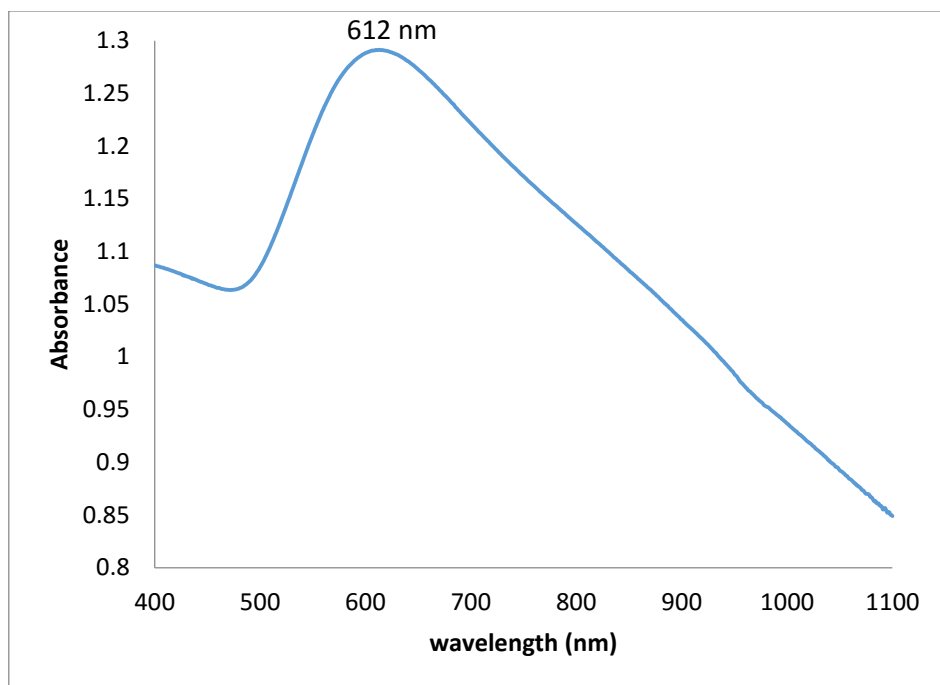
Figure 23. UV Vis absorbance result of 9 layered nanorod (Both Au and Co is short).

The peak was observed at around 622nm (Fig 24) for the nanorods with 11 layers in total (6Au and 5Co layers). The Au and Co layer thickness in these particles were about 15 and 10 nm respectively and the total rod length was about 140nm (fig 18). The peak was a little broader which suggests that all the particles were not exactly of the same length and diameter. From SEM images it was be seen that the particle lengths could vary by up to 20 nm in total length from each other.
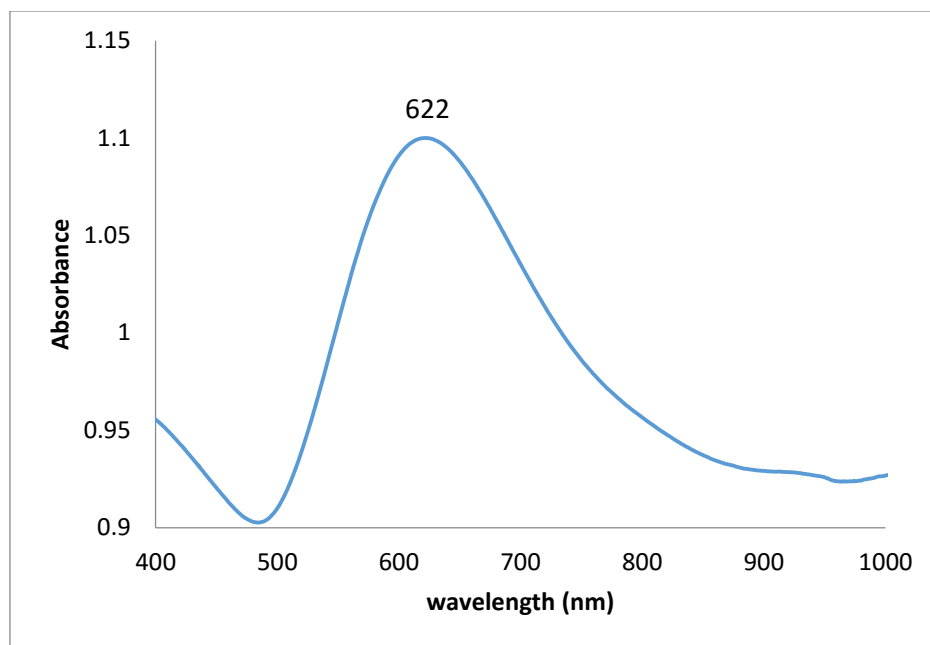
Figure 24. UV Vis absorbance result of 11 layered nanorods (both Au and Co is short).

For the 31 layered samples (Fig19) the peak was observed at 608 nm (Fig.25). These particles were about 390 nm with each Au and Co layer as about 15 and 10 nm respectively. It can be seen from the fig 22, 23 and 24 that the increase in the number of total layers in a nanorod doesn't cause a significant shift in the absorbance peak position if the individual layer thicknesses of Au and Co is maintained same in all of them.
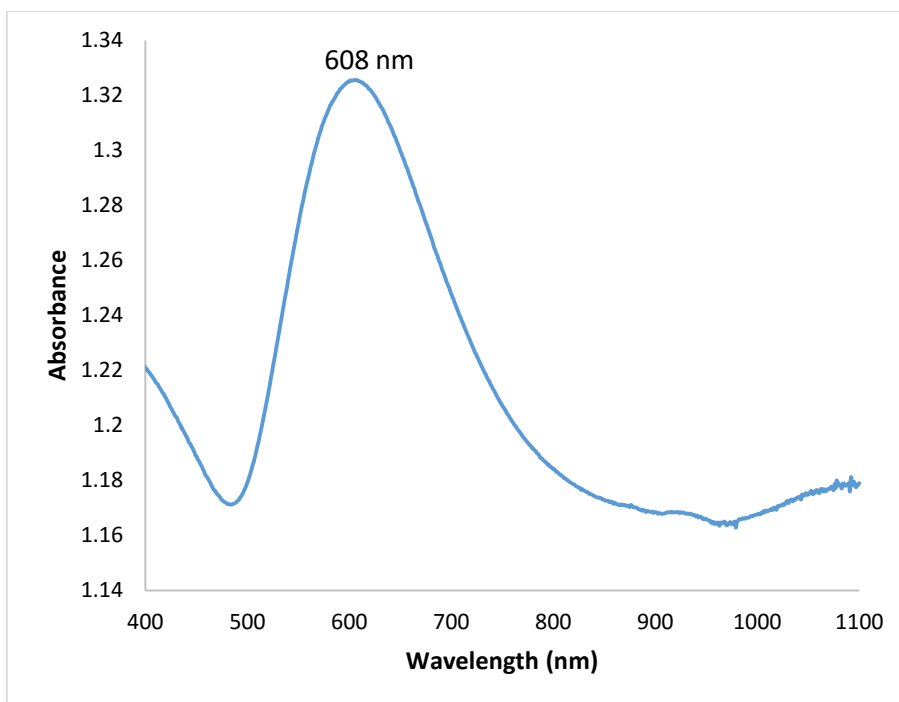
Figure 25. UV Vis absorbance result of 31 layered nanorod (Both Au and Co is short).

Next group of particles measured were 5 Au 4 Co layered nanorods with long Co segments. Here, the total particle length was roughly 515 nm (Fig 20) with each Au layer about 15 nm thick and each Co layer is about 110 nm thick. The absorbance peak is positioned at 590 nm (Fig. 26) which is even more shift than the previous 9 layered short samples (Fig 25).
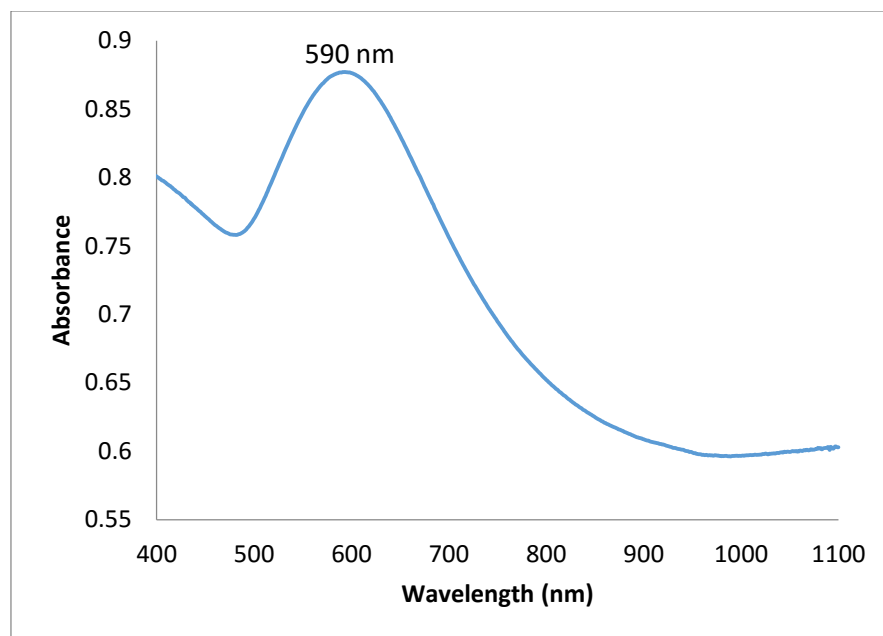
Figure 26. UV Vis absorbance result of 9 layered nanorod (short Au and long Co).

Finally, the absorbance result for 9 Layered nanorods (long Au and short Co) revealed that the peak was present at 585 nm (fig.27). The total length of these nanorods was 435 nm and individual Au and Co thicknesses were 75 and 15 nm respectively (Fig.21). The individual Au layer must show a rod like behavior (aspect ratio is 1) and the plasmon peak for rod of aspect ratio 1 should be 520 nm. The peak shift from 520 to 585 can be credited to the coupling effect between individual Au layers as they are very close to each other (~15nm)[38].
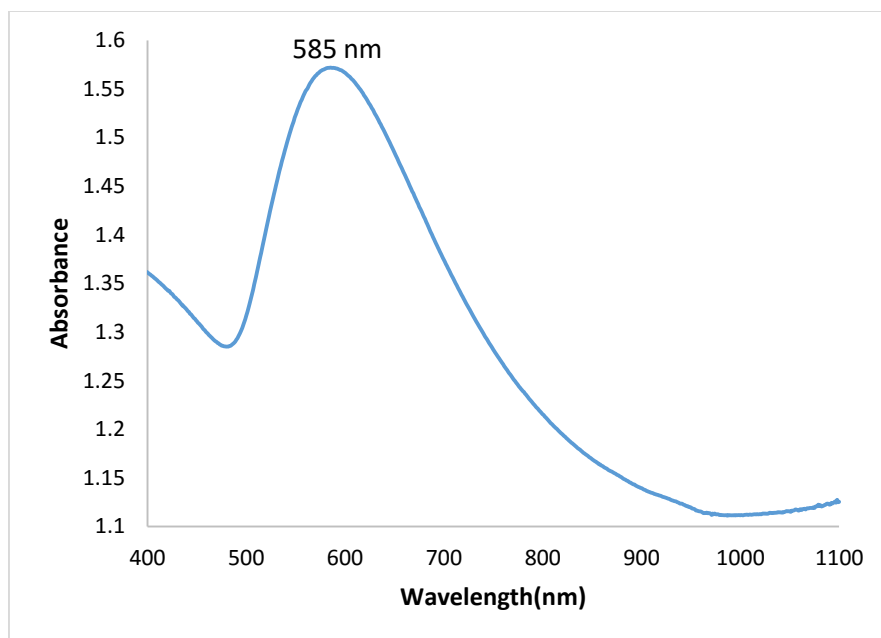
Figure 27. UV Vis absorbance result of 9 layered nanorod (long Au and short Co).

Few other nanoparticles were also synthesized by using polycarbonate membranes as the templates, but they didn't show the expected absorbance peak. (Fig 28). Those samples didn't show any visible peak. Instead, the absorbance value decreased from larger wavelength to the smaller wavelength in the spectrum range. This could be the result of undissolved polycarbonate membrane coat left around the nanoparticles even after they are dissolved in dichloromethane and then suspended in water. It could also have been the case that the peak was present outside the wavelength range measured here. But this assumption is very far-fetched as the dimensions of the synthesized multilayered nanorods were similar to that of the ones synthesized with AAO membranes (which showed the peak at around 600nm) and thus should have their absorbance peak within the same range. The only noticeable difference here is that the particles are coated with polycarbonate on their exterior. But still, a wider range of wavelength spectrum

for measurement could help to confirm this assumption about their absorbance peak.
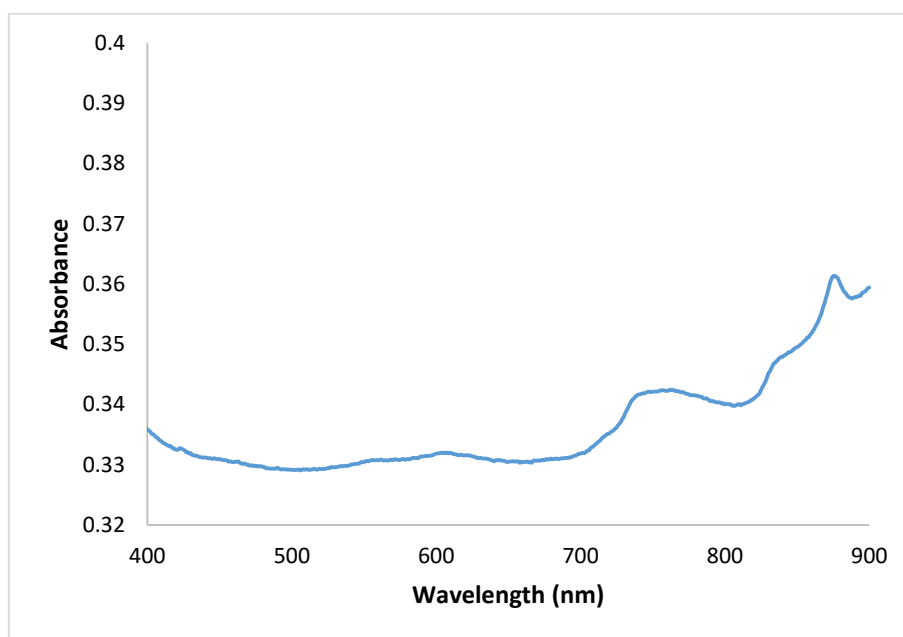

Figure 28. UV Vis result of 11 layered short multilayered nanorods using polycarbonate as a template.

4.2 MAGNETIC PROPERTIES OF MULTILAYERED NANORODS

Magnetic properties of multilayered nanorods were measured using vibrating sample magnetometer (VSM). The nanorods for VSM measurements were present inside the template that was directly used after electrodeposition of multilayers followed by washing with DI water. The templates with nanorods still inside them were cut into squares of roughly 5 mm x 5 mm and fixed on a glass rod for the VSM measurements. The external field was applied from 10000 to -10000 Oe and back again tracing a loop. The hysteresis loops were measured with

magnetic field in two direction, first parallel to the axis of the multilayered nanorod axis and then perpendicular to the axis of the rod.

From Fig 29, 30 and 31 it is clear that the hysteresis along the parallel and perpendicular field direction to the rods axis is more or less the same for the multilayered nanorods with short Au and Co layers (Fig 17 to 19). It can been also be seen that the slope of the perpendicular field hysteresis curve is slightly larger than parallel field which is expected as the easy axis for magnetization is along the disc diameter for the disc shaped Co. It can also be seen that there is no significant effect on the magnetic behavior with increase in number of total layers from 9 to 31.
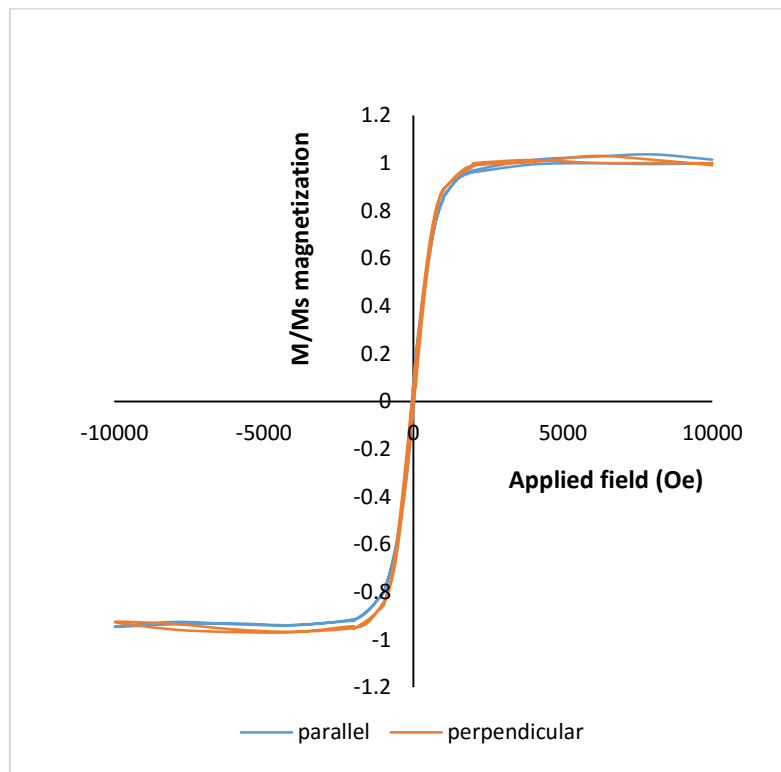

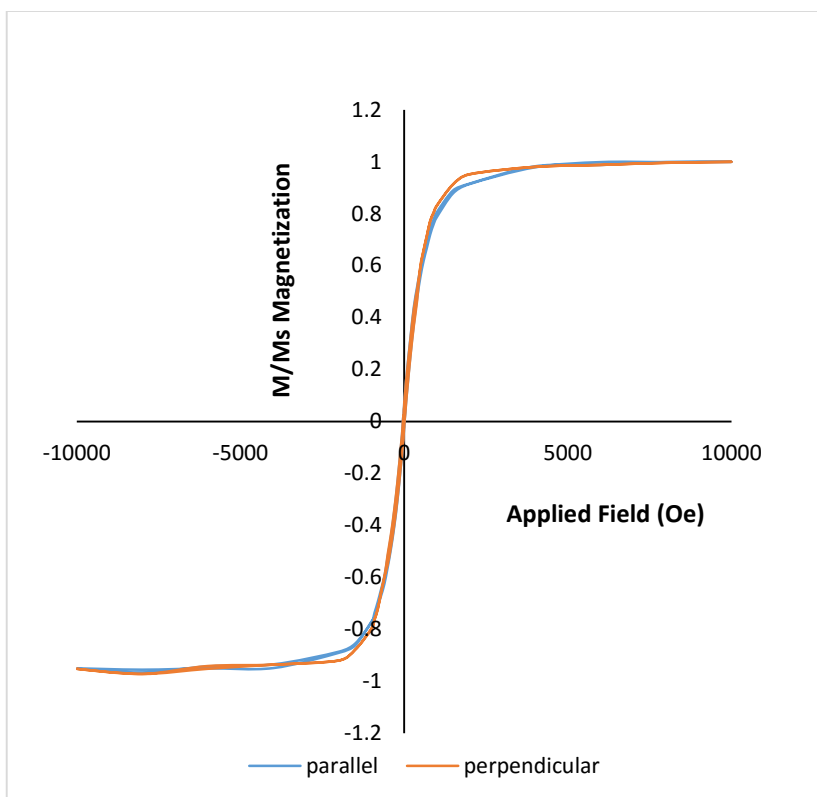Figure 29. VSM result of 9 layered nanorod (Both Au and Co is short).

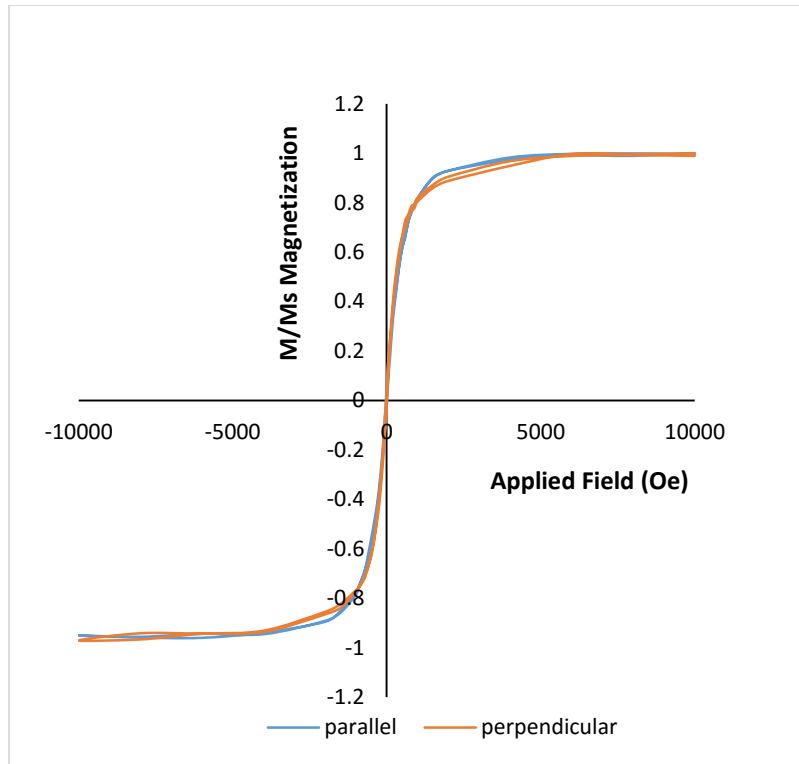Figure 30. VSM result of 11 layered nanorod (Both Au and Co is short).

Figure 31. VSM result of 31 layered nanorod (Both Au and Co is short).

Fig. 32 shows the hysteresis loop for the 9 layered nanorods (short Au and long Co). It shows very small values of remanence and coercivity (<100 Oe) (which is similar to the nanorods with short Au and Co segments before). This is desirable for the biomedical applications, because low remanence can prevent the particles from agglomerating. It can also be seen that they reach saturation magnetization at very low applied fields. The magnetic behaviors are different when the direction of external applied field is changed with respect to the particle axis. This can be seen in the hysteresis loops with applied field parallel and perpendicular to the nanorod axis (Fig. 32). It can be seen that achieving the saturation magnetization can be relatively easier if the field is parallel to the rod axis than when the field is perpendicular to the rod axis. This behavior can be explained by the shape

anisotropy of the particles. In this case the Co segment is about 100nm in length and 80 nm in diameter and so it shows a rod like behavior. The easy axis of that long Co segment lies along the axis of the segment and hence it is easier to be magnetized along the axis of the segment i.e. along the rod axis.
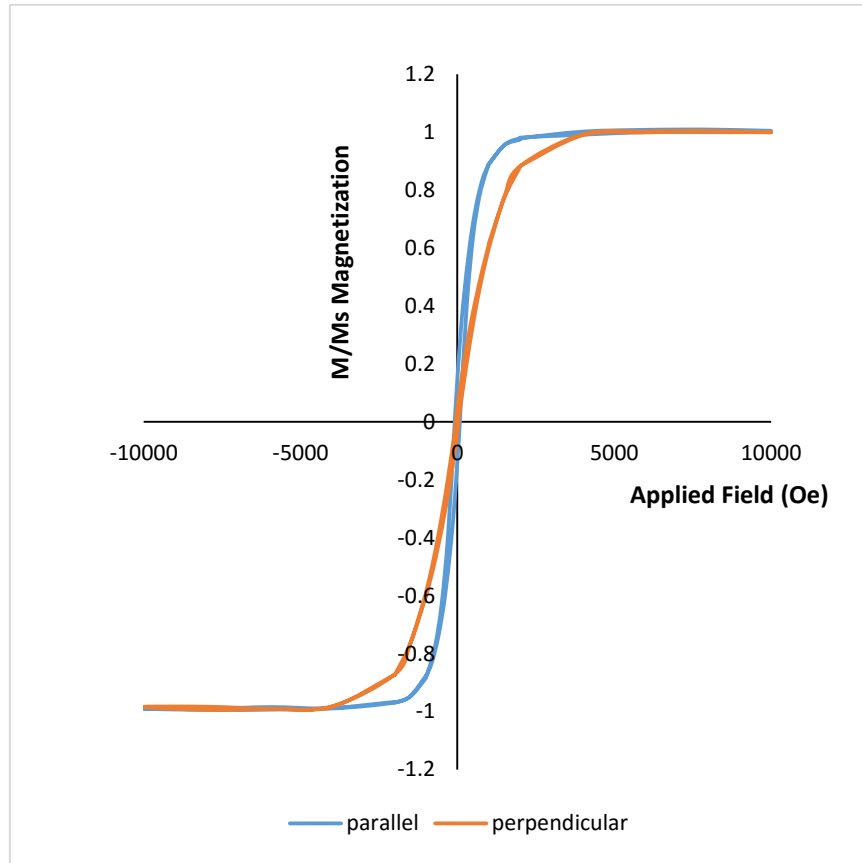

Figure 32. VSM results of 9 layered nanorods (short Au and long Co).

For the nanorods with long Au and short Co it was expected that perpendicular field should have higher slope in the hysteresis loops measured. The results are in agreement to this expectation (Fig. 33) as the easy axis for disc shaped Co is along its diameter (i.e. perpendicular to the rod). Here the individual Co discs are separated far away from each other (due to thicker Au layers) than 9,

11 and 31 layered nanorods (Fig. 29, 30 and 31) and so the shape anisotropy effect can be seen more pronounced in Fig. 33.
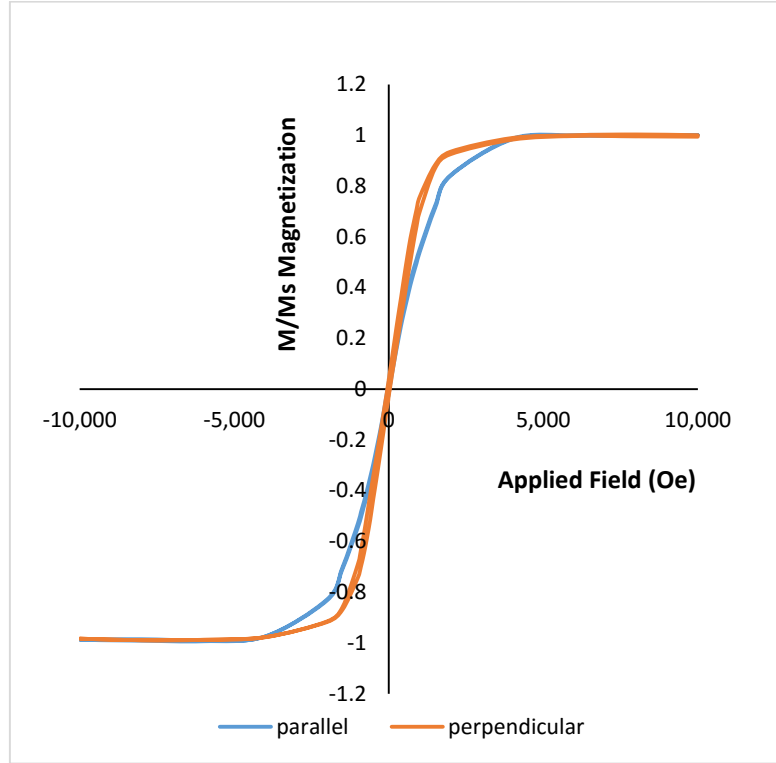

Figure 33. VSM results of 9 layered nanorods (long Au and short Co).

Also, for the rods with longer Co segments the easy axis was the rod axis and the individual magnetizations of the segments could be arranging in the same direction (fig. 34) which could thus be helping for magnetization along the rods axis (Fig32). But for the rods with shorter Co segments, the individual magnetizations of each segments could be aligning in the antiparallel direction (in the perpendicular direction to the rod axis) (Fig. 34) and thus should be reducing the difference between the parallel and perpendicular loops (Fig. 29, 30 and 31). The VSM results found in this study are similar to another study [39].
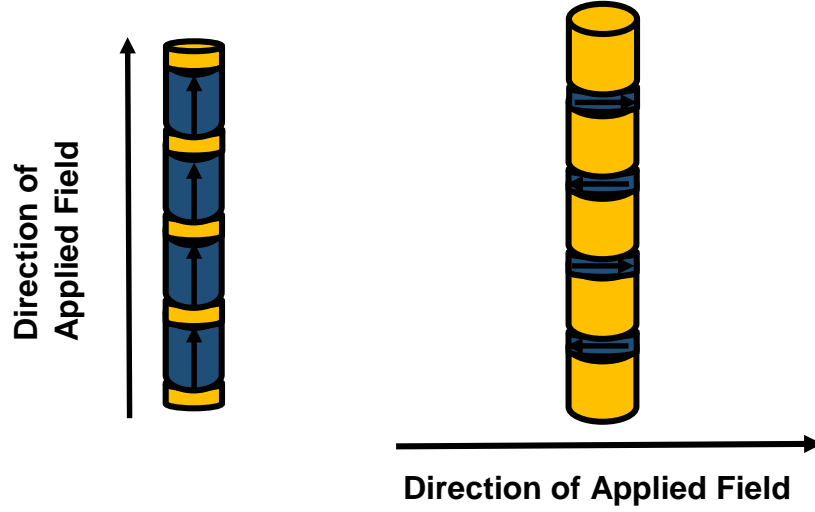
Figure 34. Schematic of the individual magnetization alignment in disc shaped and rod shaped Co segments.

4.2.1 ANISOTROPY ENERGY AND COERCIVITY DETERMINATION

The magnetostatic energy can be calculated [40] by using the equation (14), where Nd is the demagnetization factors. The saturation magnetization (M_s) for Co is 1422 emu/cm^3. N_d can be calculated from equations (15), (16), (17) and (18) and it varies with dimensions of the Co segments. We approximate a rod as a prolate spheroid (equation 15 and 16) and a disk or as an oblate spheroid (equation 17 and 18). The illustrations for prolate (rod like) and oblate (disc like) spheroids are shown in Fig. 35.

$$E_d = \frac{1}{2} N_d M_s^2 \qquad\qquad (14)$$

$$N_a = N_b = 4\pi \frac{m}{2(m^2 - 1)} \times \left[m - \frac{1}{2(m^2 - 1)^{1/2}} \times \ln \left(\frac{m + (m^2 - 1)^{1/2}}{m - (m^2 - 1)^{1/2}} \right) \right] \qquad (15)$$

$$N_c = 4\pi \frac{1}{(m^2 - 1)} \times \left[\frac{m}{2(m^2 - 1)^{1/2}} \times \ln \left(\frac{m + (m^2 - 1)^{1/2}}{m - (m^2 - 1)^{1/2}} \right) - 1 \right] \qquad (16)$$

$$N_a = 4\pi \frac{m^2}{(m^2 - 1)} \times \left[1 - \frac{1}{(m^2 - 1)^{1/2}} \times \sin^{-1} \left(\frac{(m^2 - 1)^{1/2}}{m} \right) \right] \qquad (17)$$

$$N_c = N_b = 4\pi \frac{1}{2(m^2 - 1)} \times \left[\frac{m^2}{(m^2 - 1)^{1/2}} \times \sin^{-1} \left(\frac{(m^2 - 1)^{1/2}}{m} \right) - 1 \right] \qquad (18)$$
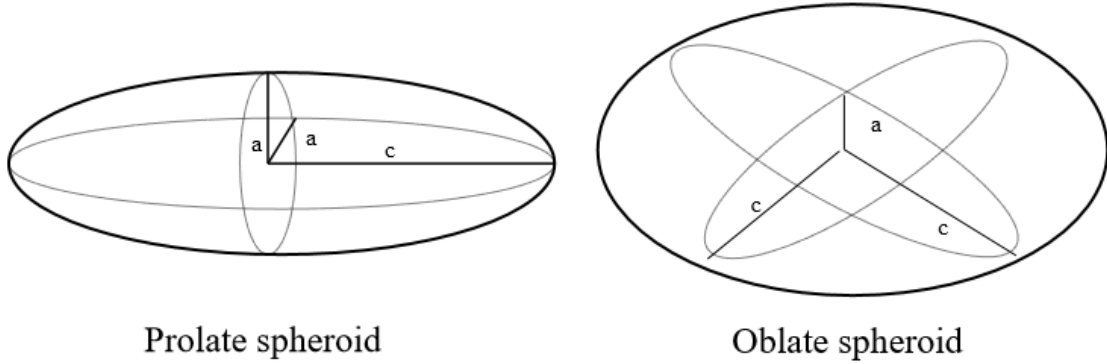

Figure 35. Schematic illustration of prolate spheroid and oblate spheroid.

By substituting m = c/a = 50/40 = 1.25 (i.e. dimensions of Co segment for 9 layered Long multilayered nanorod), the demagnetization factors are calculated from equations (15) and (16) as

(Prolate): N_a = N_b = 4.55 (hard axis) and N_c = 3.4695 (easy axis)   (19)

And by substituting m= c/a = 40/6.5 = 6.15 in equations (17) and (18) (i.e. dimensions of disc shaped Co segments for 9 layered short multilayered nanorods) we get,

(Oblate): N_a = 9.914 (hard axis) and N_b = N_c = 1.326 (easy axis)   (20)

Using these demagnetization factor values (i.e. equations (19) and (20)), the magnetostatic energies along different directions can be calculated by using equation (14) as,

For rod like Co segment:

(Easy axis) Parallel to rod axis (c axis) E_d = 3.5 x 10^6 erg/cm^3

(Hard axis) Perpendicular to rod axis (a axis) E_d = 4.6 x 10^6 erg/cm^3

For disc like Co segment:

(Easy axis) Perpendicular to rod axis (c axis) E_d = 1.34 x 10^6 erg/cm^3

(Hard axis) Parallel to rod axis (a axis) E_d = 10.02 x 10^6 erg/cm^3
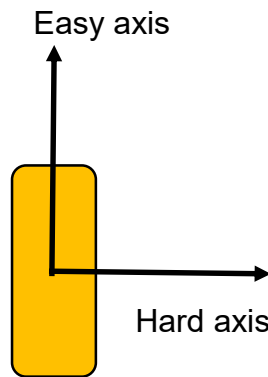

Figure 36. Schematic diagram of magnetization for an elongated nanoparticle

The shape anisotropy energy can be considered as the difference between the magnetostatic energies along hard axis and easy axis (Fig. 36). The shape anisotropy energy when the magnetization is rotated from easy axis to hard axis

(i.e. by 90^0) can be calculated by using $\frac{1}{2} M_s^2 (N_a - N_c)$ (using eqn 14) which can also be expressed using $E_{ani} = K_0 + K_1 \sin^2\theta + \ldots$ and so we get,

$$\frac{1}{2} M_s^2 (N_a - N_c) = E_{ani} (90^0 - 0^0) = K_1 \qquad (21)$$
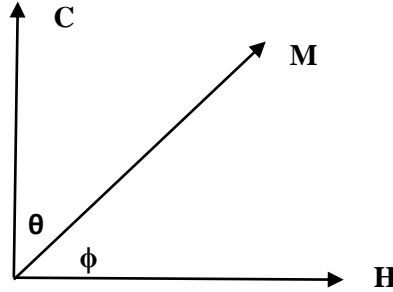

Figure 37. Schematic relation between the easy axis, the applied field and magnetization directions.

In an applied field, total energy is the sum of magnetic potential energy (E_H) and anisotropy energy. I.e. $E_T = E_H + E_{ani}$. Thus, the direction of the magnetization will be determined when the total energy is minimum. The total energy can be written as,

$E_T = - MH\cos\phi + K_1 \sin^2\theta + K_0$

With $\theta + \phi = 90^o$

$E_T = - MH\sin\theta + K_1 \sin^2\theta + K_0$

Differentiating the above equation with respect to θ we get,

$dE_T / d\theta = 0 = - MH\cos\theta + 2K_1 \sin\theta\cos\theta$

So, $H = 2K_1 \sin\theta / M$

$\theta = 90$ is when the magnetization points to hard axis, and the field is the saturation field for the hard axis in hysteresis loop. We get,

$$H = 2K_1 / M_s \qquad (22)$$

Now this field is also the coercivity when applied field is parallel to the easy axis.

Using (21), (22) and $M_s = 1422$ emu/cm^3 we can calculate H_c as given below,

For rod like Co segments (prolate):

$K_1 = 0.5 \times (1422)^2 \times 1.0805 = 1.0924 \times 10^6$ erg/cm^3

$$H_c = 2 \times 1.0924 \times 10^6 / 1422 = 1536.43 \text{ Oe} \qquad (23)$$

For disc like Co segments (oblate):

$K_1 = 0.5 \times (1422)^2 \times 8.588 = 8.68283 \times 10^6$ erg/cm^3

$$H_c = 2 \times 8.68283 \times 10^6 / 1422 = 12212.14 \text{ Oe} \qquad (24)$$

It can be seen that the H_c values calculated here are much higher than the experimentally measured values (for the multilayered rods).
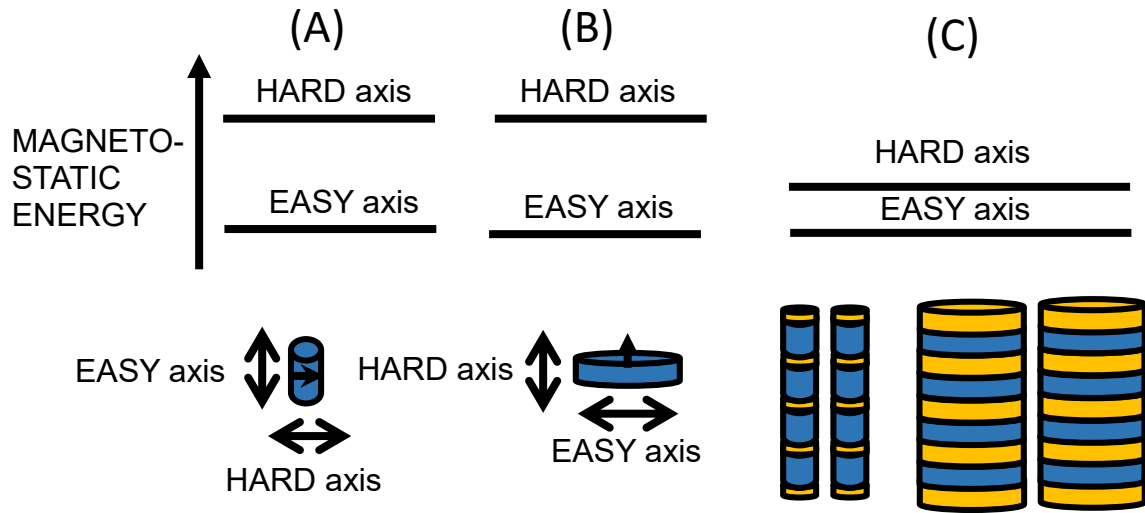
Figure 38. Schematic drawing of suppression effect.

For individual elongated structures, like these nanorods, a large shape anisotropy exists with easy axis along long axis, as calculated above. But, in densely packed arrays, this shape anisotropy for individual rods is almost completely suppressed. Shape anisotropy can be viewed as the magnetostatic energy difference between magnetization along long axis and short axis (Fig. 38). The magnitude of magnetostatic energy is assessed as the volume of space into which the magnetic field permeates. In densely packed arrays, when magnetization points to short axis, magnetic field originated from one rod quickly end to its neighbors, almost no magnetic field spreads out, so magnetostatic energy along this direction dramatically decreases (Fig 38). This results in the suppression of shape anisotropy. In a closely packed array, each rod can be treated as one domain and all rods are coupled together, similar to multidomain thin films. However, the magnetization switching mechanism is totally different from thin films since "domain walls" are fixed for the rod/tube array, and the "domain

64

propagation" can only be through magnetostatic interaction. The out-of-plane saturation fields measure this magnetostatic energy when all magnetization point along long axis, which is proportional to the magnetic moment of each tube/rod.
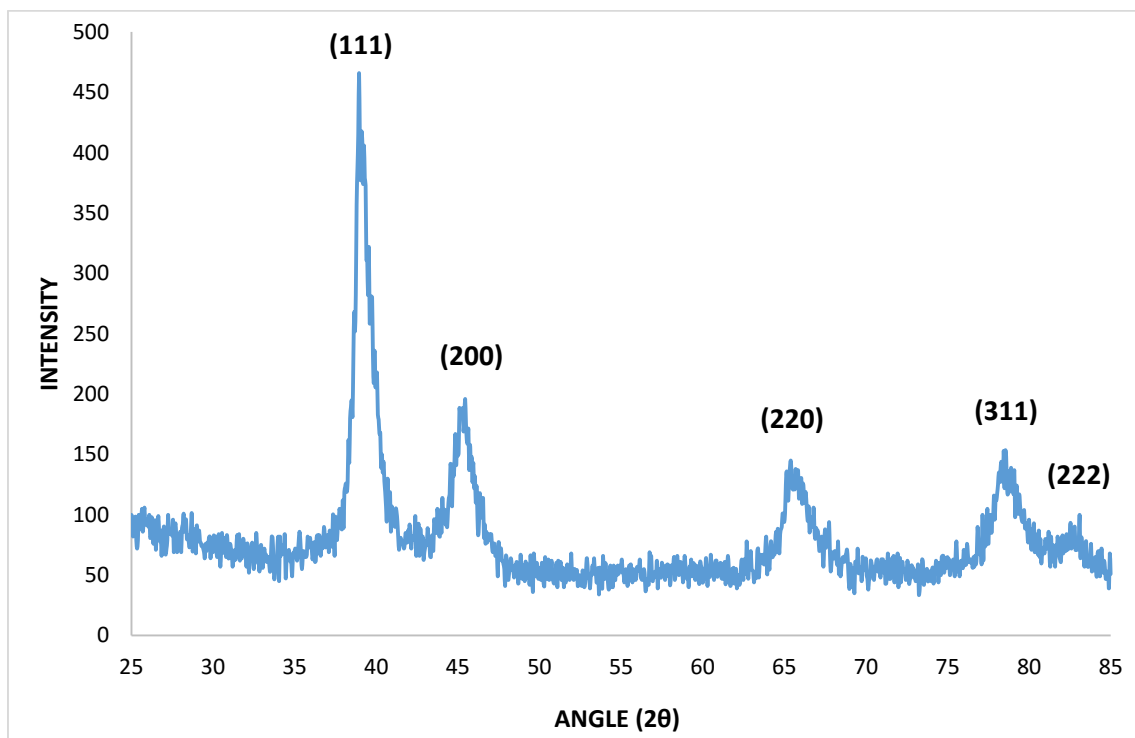
4.3   CRYSTAL STRUCTURE DETERMINATION

Figure 39. XRD graph (I vs 2θ) for all types of particles mixed into one sample.

The above graph was obtained by mixing all kinds of samples made in this study (multilayered nanorods with thicker Co or Au or that have both layers of Au and Co as discs) to verify the crystal structure of Au and Co after electrodeposition. When Fig 39 is compared for peak positions with std XRD results for Au nanorods (Fig 40) it can be seen that the peak positions match with each other. Thus it can be believed that the results show a FCC structure which is Au.
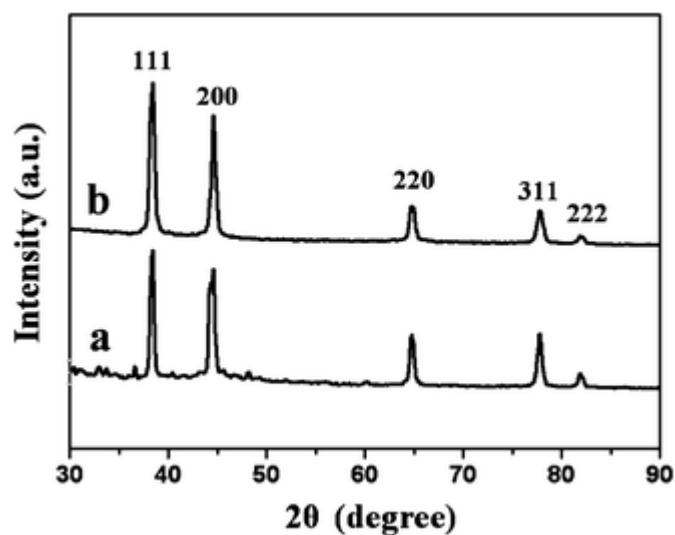
Figure 40. XRD of FCC Au nanorods.

Comparing Fig 41 to Fig 39 it seems that the peaks for std FCC Co don't seem to be there in the sample XRD (Fig 39). The Co was expected to be FCC as it grows on a FCC Au substrate. The absence of FCC peaks in the measured XRD sample suggest that the Co was amorphous which might have been the results of

very high rate of Co during pulse electrodeposition. The presence of Co is certain as the VSM results show the samples to be very magnetic.

So looks like we have both Au and Co with Au as FCC and Co as amorphous.

Figure 41. XRD of Co with different types of crystal structures.

5   SUMMARY
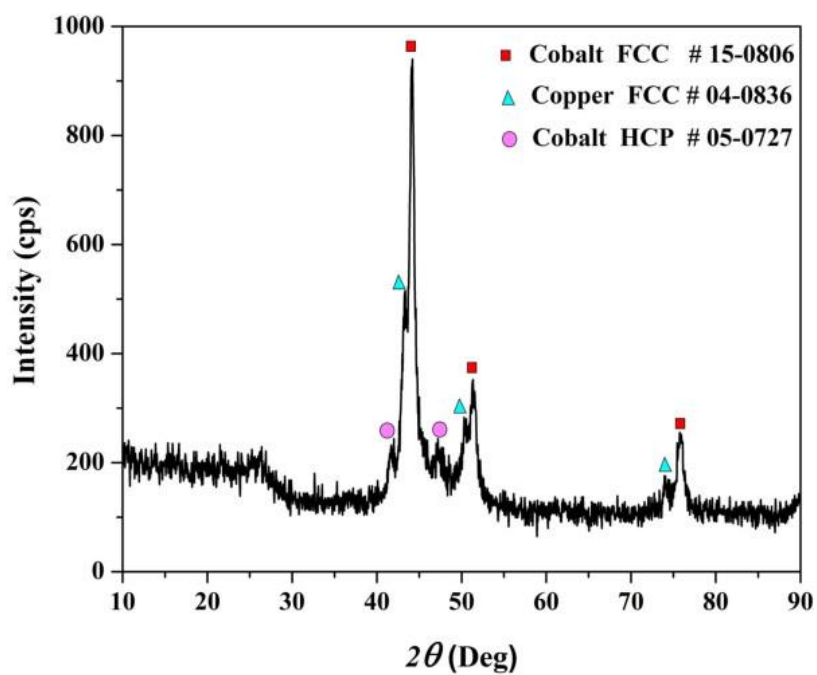
The Au-Co multilayered nanorods were proposed to combine both SPR and magnetic properties for biomedical applications. The presence of SPR peak in the NIR range is beneficial for deep penetration into the tissue without damaging it and reaching the treatment sites underneath. The Au layer can also be used as bonding sites for molecules that need to be carried to the treatment area. The magnetic part in the nanorods can act as MRI contrast agent for diagnostic imaging. Thus such single type of particle can be used both for diagnostic and therapeutic purposes.

The multilayered nanorods were successfully synthesized by template electrodeposition. Anodic aluminum oxide (AAO) membrane with through channels were used as templates, and were fabricated by anodizing thin Al foils in 0.23M oxalic acid   for 6hrs at 40V. The synthesized templates were about 10 µm in thickness and had uniform channels of about 80nm in diameters from top to bottom.

The multilayered nanorods with disc like Au (15 nm) and Co (10 nm), longer Au (75nm) and longer Co (110nm) segments were synthesized. The templates were coated with Cu by evaporation on one side to serve as working electrode in electrodeposition. The electrodeposition of Cu, Au and Co was carried out by using a 3 electrode cell. The sacrificial Cu was first electrodeposited in the channels by using dilute acidic Cu sulfate solution at -0.1 V vs Ag/Ag chloride reference electrode. The multilayered Au-Co nanorods were synthesized by pulse electrodeposition technique using a single bath electrolyte at different applied potentials (Au at -0.7 and Co at -1.1V vs Ag/ AgCl). In the single bath electrolyte,

Co ion concentration is much higher than Au ion concentration, which make it possible to deposit Co segment without incorporating too much Au. Such templated electrodeposition technique generates a large number of particles at once and it is simple to carry out than other techniques like lithography.

The optical properties of multilayered nanorods were characterized by measuring the absorption spectra of nanorod water suspension. The absorption spectra for all the samples showed a clear single peak in the scanned range of 400 nm to 100 nm. It has been found that there was no significant change in the peak position when an extra layers of Au and Co were added to the multilayered nanorods with disc shaped Au and Co layers. The peak shifted to the blue side when the thickness of the Co layer was increased to 110nm and when thickness of Au was increased to 75 nm keeping the total number of layers to be 9 in both cases. The peak shift to about 590nm could be the result of intercoupling between neighboring Au discs or Au rods.

Magnetic properties of the multilayered nanorods were characterized by measuring hysteresis loops of nanorods inside the membrane using a vibrating sample magnetometer. The results showed that the remanence and coercivity (<100 Oe) were very small for both types of multilayered nanorods (with rod like and disk like Co segments), but possessed a large saturation magnetization. For the nanorods with rod like Co segments the magnetic easy axis was along the rod axis, and for the nanorods with disc like Co layers the easy axis was along the diameter of the rod. This behavior is credited to shape anisotropy of the Co layers in which the easy axis of a nanoparticle is set along its longest dimension. The

nanorods with disc like Au and Co segments showed a negligible anisotropy, but the nanorods with longer Au segments and disc like Co segments showed clear shape anisotropy. From theoretical calculations of shape anisotropy energy the coercivity values were calculated, which were much higher than what were seen in the measured results. This is due to the interaction between the neighboring Co layers, causing the suppression of the shape anisotropy.

6 REFERENCES

[1] J.E. Millstone, S. Park, K.L. Shuford, L.D. Qin, G.C. Schatz, C.A. Mirkin, J. Am. Chem. Soc., 127 (2005) 5312-5313.

[2] E. Boisselier, D. Astruc, Chem. Soc. Rev., 38 (2009) 1759-1782.

[3] E. Duguet, S. Vasseur, S. Mornet, J.M. Devoisselle, Nanomedicine, 1 (2006) 157-168.

[4] M. Chen, S. Yamamuro, D. Farrell, S.A. Majetich, Journal of Applied Physics, 93 (2003) 7551-7553.

[5] M. Aslam, L. Fu, S. Li, V.P. Dravid, Journal of Colloid and Interface Science, 290 (2005) 444-449.

[6] J. Bai, J.-P. Wang, Applied Physics Letters, 87 (2005) 152502.

[7] L.C. Brian, O.G. Vladimir, H. Marcia, L.O. Brittany, C. Ebony, W.H. Corey, J.O.C. Charles, Nanotechnology, 16 (2005) 1701.

[8] L. Diaz, M. Santos, C. Ballesteros, M. Marysko, J. Pola, Journal of Materials Chemistry, 15 (2005) 4311-4317.

[9] W. Fu, H. Yang, L. Chang, M. Li, H. Bala, Q. Yu, G. Zou, Colloids and Surfaces A: Physicochemical and Engineering Aspects, 262 (2005) 71-75.

[10] L. Chih-Huang, W. Tsung-Feng, L. Ming-Der, IEEE Transactions on Magnetics, 41 (2005) 3397-3399.

[11] W. Liu, W. Zhong, Y.H. Jiang, J.N. Tang, L.X. Wu, Y.W. Du, The European Physical Journal B - Condensed Matter and Complex Systems, 46 (2005) 471-474.

[12] V. Salgueiriño-Maceira, M.A. Correa-Duarte, M. Farle, Small, 1 (2005) 1073-1076.

[13] M. Hu, J. Chen, Z.-Y. Li, L. Au, G.V. Hartland, X. Li, M. Marquez, Y. Xia, Chemical Society Reviews, 35 (2006) 1084-1094.

[14] P.K. Jain, I.H. El-Sayed, M.A. El-Sayed, Nano Today, 2 (2007) 18-29.

[15] S. Link, M.A. El-Sayed, International Reviews in Physical Chemistry, 19 (2000) 409-453.

[16] K.L. Kelly, E. Coronado, L.L. Zhao, G.C. Schatz, The Journal of Physical Chemistry B, 107 (2003) 668-677.

[17] S. Link, M.B. Mohamed, M.A. El-Sayed, The Journal of Physical Chemistry B, 103 (1999) 3073-3077.

[18] N.R. Jana, L. Gearheart, C.J. Murphy, J. Phys. Chem. B, 105 (2001) 4065-4067.

[19] A.M. Gobin, M.H. Lee, N.J. Halas, W.D. James, R.A. Drezek, J.L. West, Nano Lett., 7 (2007) 1929-1934.

[20] S. Lal, S.E. Clare, N.J. Halas, Accounts Chem. Res., 41 (2008) 1842-1851.

[21] Y.G. Sun, Y.N. Xia, Science, 298 (2002) 2176-2179.

[22] J. Chen, F. Saeki, B.J. Wiley, H. Cang, M.J. Cobb, Z.Y. Li, L. Au, H. Zhang, M.B. Kimmey, X.D. Li, Y. Xia, Nano Lett., 5 (2005) 473-477.

[23] Z.C. Xu, Y.L. Hou, S.H. Sun, J. Am. Chem. Soc., 129 (2007) 8698-+.

[24] E.V. Shevchenko, M.I. Bodnarchitk, M.V. Kovalenko, D.V. Talapin, R.K. Smith, S. Aloni, W. Heiss, A.P. Alivisatos, Adv. Mater., 20 (2008) 4323-4329.

[25] I.C. Chiang, D.H. Chen, Adv. Funct. Mater., 17 (2007) 1311-1316.

[26] C.S. Levin, C. Hofmann, T.A. Ali, A.T. Kelly, E. Morosan, P. Nordlander, K.H. Whitmire, N.J. Halas, Acs Nano, 3 (2009) 1379-1388.

[27] R. Bardhan, W.X. Chen, C. Perez-Torres, M. Bartels, R.M. Huschka, L.L. Zhao, E. Morosan, R.G. Pautler, A. Joshi, N.J. Halas, Adv. Funct. Mater., 19 (2009) 3901-3909.

[28] G. Mie, Annalen der Physik, 330 (1908) 377-445.

[29] R. Gans, Annalen der Physik, 342 (1912) 881-900.

[30] H. Chen, L. Shao, Q. Li, J. Wang, Chemical Society Reviews, 42 (2013) 2679-2724.

[31] J. Pérez-Juste, I. Pastoriza-Santos, L.M. Liz-Marzán, P. Mulvaney, Coordination Chemistry Reviews, 249 (2005) 1870-1901.

[32] N.J. Halas, S. Lal, W.-S. Chang, S. Link, P. Nordlander, Chemical Reviews, 111 (2011) 3913-3961.

[33] I. Zorić, M. Zäch, B. Kasemo, C. Langhammer, ACS Nano, 5 (2011) 2535-2546.

[34] M.N. O'Brien, M.R. Jones, K.L. Kohlstedt, G.C. Schatz, C.A. Mirkin, Nano Letters, 15 (2015) 1012-1017.

[35] W. Lee, R. Ji, U. Gosele, K. Nielsch, Nat Mater, 5 (2006) 741-747.

[36] G.D. Sulka, Highly Ordered Anodic Porous Alumina Formation by Self-Organized Anodizing, Nanostructured Materials in Electrochemistry, Wiley-VCH Verlag GmbH & Co. KGaA, 2008, pp. 1-116.

[37] T. Aerts, I. De Graeve, H. Terryn, Electrochimica Acta, 54 (2008) 270-279.

[38] A.M. Funston, C. Novo, T.J. Davis, P. Mulvaney, Nano Letters, 9 (2009) 1651-1658.

[39] S. Valizadeh, L. Hultman, J.M. George, P. Leisner, Advanced Functional Materials, 12 (2002) 766-772.

[40] L. Sun, Y. Hao, C.L. Chien, P.C. Searson, IBM Journal of Research and Development, 49 (2005) 79-102.